

Bi-fidelity Variational Auto-encoder for Uncertainty Quantification

Nuojin Cheng^a, Osman Asif Malik^b, Stephen Becker^a, Alireza Doostan^c

^a*Department of Applied Mathematics, University of Colorado, Boulder,*

^b*Applied Mathematics & Computational Research Division, Lawrence Berkeley National Laboratory,*

^c*Ann and H.J. Smead Department of Aerospace Engineering Sciences, University of Colorado, Boulder,*

Abstract

Quantifying the uncertainty of quantities of interest (QoIs) from physical systems is a primary objective in model validation. However, achieving this goal entails balancing the need for computational efficiency with the requirement for numerical accuracy. To address this trade-off, we propose a novel bi-fidelity formulation of variational auto-encoders (BF-VAE) designed to estimate the uncertainty associated with a QoI from low-fidelity (LF) and high-fidelity (HF) samples of the QoI. This model allows for the approximation of the statistics of the HF QoI by leveraging information derived from its LF counterpart. Specifically, we design a bi-fidelity auto-regressive model in the latent space that is integrated within the VAE's probabilistic encoder-decoder structure. An effective algorithm is proposed to maximize the variational lower bound of the HF log-likelihood in the presence of limited HF data, resulting in the synthesis of HF realizations with a reduced computational cost. Additionally, we introduce the concept of the bi-fidelity information bottleneck (BF-IB) to provide an information-theoretic interpretation of the proposed BF-VAE model. Our numerical results demonstrate that BF-VAE leads to considerably improved accuracy, as compared to a VAE trained using only HF data, when limited HF data is available.

Keywords: uncertainty quantification, variational auto-encoder, multi-fidelity, generative modeling, transfer learning

1. Introduction

Uncertainty pervades numerous engineering applications owing to various factors such as material properties, operating environments, and boundary conditions, which affect the prediction of a performance metric or quantity of interest (QoI), $\mathbf{x} \in \mathbb{R}^D$, following an (unknown) density $p(\mathbf{x})$. The quantification of uncertainty in \mathbf{x} through the estimation of its moments or distribution has been an active area of research within the field of uncertainty quantification (UQ). One approach to accomplish this involves the collection of independent and identically distributed (i.i.d.) realizations of \mathbf{x} to estimate its empirical properties. However, when the realizations of \mathbf{x} are obtained through the solution of computationally intensive models, generating a large enough set of realizations to ensure statistical convergence becomes infeasible. To alleviate this challenge, a surrogate model of the forward map between uncertain inputs $\boldsymbol{\xi} \in \mathbb{R}^M$ and \mathbf{x} can be constructed. This approach has been demonstrated

through a range of techniques, including polynomial chaos expansion [1, 2, 3, 4], Gaussian process regression [5, 6], and deep neural networks [7, 8, 9, 4]. Once established, the surrogate model can be employed, often at a negligible cost, to generate realizations of the QoI and estimate its statistics. However, it should be noted that the complexity of constructing these surrogate models often increases rapidly with the number of uncertain variables M , a phenomenon referred to as the curse of dimensionality.

To mitigate the problem caused by high-dimensional uncertainty, one solution is using reduced-order models (ROMs) [10], which seek to project the governing equations of forward models onto a subspace of lower dimensionality. The reduced subspace is established through a set of basis vectors of size possibly independent of the dimensionality of uncertainty. One widely adopted technique for identifying this subspace is proper orthogonal decomposition (POD), also referred to as principle component analysis (PCA) or Karhunen–Loève expansion [11]. POD is commonly employed on a collection of forward problem simulations, known as snapshots, to determine the optimal subspace via the solution of a singular value decomposition problem.

The utility of ROMs has been extensively investigated for diffusion-dominant problems that exhibit faster decay in Kolmogorov n -width [12]. However, for advective-dominated problems where solutions are not close to any linear subspace, conventional ROMs can produce inaccurate approximations. This has resulted in the increasing popularity of manifold-based ROMs, including kernel principal component analysis [13, 14], tangent space alignment [15], and auto-encoders (AE) [16, 17, 18]. Of these manifold-based ROMs, AE has gained significant attention because its expressive neural-network-based encoder-decoder structure is able to capture the underlying patterns of the input data by learning a latent representation. The latent representation, denoted by \mathbf{z} , is of much lower dimension than the input data and is learned through a non-linear encoder function. The decoder function, which typically has a structure mirroring the encoder function, takes the learned latent representation \mathbf{z} and maps it back to the original data space.

While AE-based UQ models [16, 17, 18] have demonstrated success in physical modeling, they do not use a Bayesian framework to capture the stochasticity inherent to the UQ problems. In addition, as demonstrated by [19], the lack of regularization of the fully-connected AE architecture can result in overfitting to an identity map and hinder the discovery of meaningful latent representations. To address these limitations, many probabilistic UQ frameworks are proposed to regularize the problem and, more significantly, enable uncertainty estimation. Previous studies have utilized a Bayesian convolutional AE [20] specifically for flow-based problems and an auto-regressive encoder-decoder structure for turbulent flows [21].

In this study, we present a novel, non-intrusive training strategy for uncertainty estimation in physical systems by leveraging the capability of the variational autoencoder (VAE). The VAE framework represents a class of machine learning models that seek to approximate the unknown underlying distribution from which the QoI of a system is derived, and generate new realizations from it. Deep generative models, including VAE [22, 23], generative adversarial networks (GAN) [24], normalizing flows [25], and diffusion models [26, 27], have

garnered substantial success in diverse applications in computer vision and natural language processing [28, 29, 30]. VAE, in particular, offers a remarkably apt solution for UQ problems, owing to its ability to encode a low-dimensional representation of the QoIs, generate new realizations, and regularize the model via its probabilistic formulation. Further details on the VAE methodology can be found in Section 2.1.

Despite the potential benefits, training deep generative models, such as VAEs, necessitates access to a substantial amount of accurate high-fidelity (HF) data. In our study, we adopt a bi-fidelity approach, where limited realizations of the HF QoI $\mathbf{x}^H \in \mathbb{R}^D$ and a larger set of cheaper but less accurate realizations of corresponding low-fidelity (LF) QoI $\mathbf{x}^L \in \mathbb{R}^D$ are available. By involving the LF QoI and conducting a regression between LF and HF variables, the proposed model is independent of the stochastic input dimension and overcomes the curse of dimensionality. We construct a probabilistic model, primarily trained on LF realizations, that captures the underlying distribution of the HF QoI.

By incorporating the VAE structure, we are able to perform regression between LF and HF models in a lower-dimensional latent space, significantly reducing the number of HF samples required for training. This is accomplished by introducing latent variables $\mathbf{z}^L, \mathbf{z}^H \in \mathbb{R}^d$ and an auto-regression $p_\psi(\mathbf{z}^H|\mathbf{z}^L)$ parameterized by ψ to capture the relationship between the LF and HF models in the latent space, instead of a direct regression in the high-dimensional observation space, as depicted in Figure 1. An encoder $q_\phi(\mathbf{z}^L|\mathbf{x}^L)$ trained by LF data and a decoder $p_\theta(\mathbf{x}^H|\mathbf{z}^H)$ firstly pre-trained by LF data and then tuned by HF data are provided to map the data between the observation space and latent space. Our results show that a relatively small set of HF realizations are enough to recover HF QoI at a reasonable accuracy level.

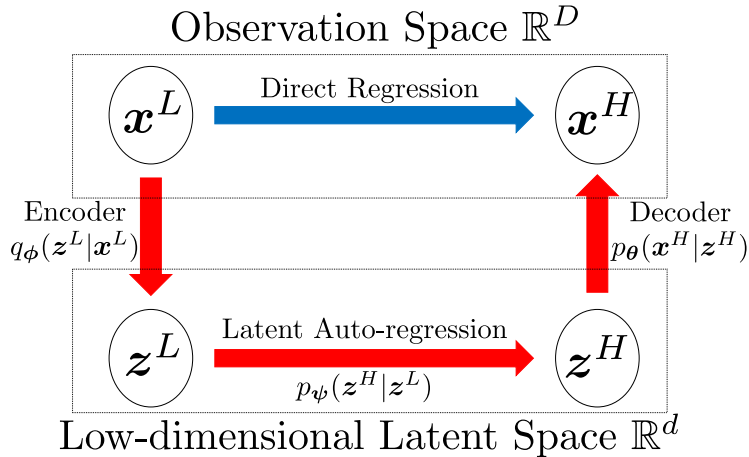


Figure 1: Instead of conducting bi-fidelity regression directly in high-dimensional observation space (blue path), we introduce an approach via low-dimensional latent space (red path).

To summarize, the core contributions of this work are:

- We introduce a bi-fidelity variational autoencoder (BF-VAE) model and an algorithm, Algorithm 1, to train the BF-VAE in the presence of scarce HF data. The trained model effectively captures the distribution of the high-dimensional random vector \mathbf{x}^H , thereby enabling the generation of new HF QoI realizations.
- The BF-VAE model is theoretically motivated as the minimizer of a training objective criterion we call BF-ELBO. We then extend the information bottleneck theory of Tishby et al. [31] to formulate the bi-fidelity information bottleneck (BF-IB) theory and provide an interpretation of BF-ELBO from an information-theoretic perspective.
- We conduct an empirical evaluation of the BF-VAE model through three numerical experiments, comparing its performance with the standard VAE method. The numerical results indicate that BF-VAE improves the accuracy of learned HF QoI when the number of HF data is small.

The rest of the paper is structured as follows. In Section 2, we provide an overview of the VAE and linear auto-regressive methods for bi-fidelity regression. Section 3 elaborates on the proposed BF-VAE model, along with a theoretical interpretation. The implementation details of the BF-VAE model, including prior density selection and hyperparameter tuning, are presented in Section 4. Section 5 showcases three numerical examples that demonstrate the performance of BF-VAE. Our conclusions are summarized in Section 6. The proof of our main statements and an introduction to an implemented evaluation metric are presented in the appendix. For consistency with other VAE-related papers, we do not differentiate random vectors and their realizations in this work. Additionally, we simplify density functions by omitting their subscripts. For example, we use $p(\mathbf{x}|\mathbf{y})$ instead of $p_{\mathbf{x}|\mathbf{y}}(\mathbf{x}|\mathbf{y})$.

2. Motivation and Background

Forward UQ is a topic about addressing the issue of uncertainty in mathematical models that arise from modeling physical systems. Under the bi-fidelity setting, an HF numerical model generates HF QoI $\mathbf{x}^H \in \mathbb{R}^D$ with density $p(\mathbf{x}^H)$ and an LF numerical model generates LF QoI $\mathbf{x}^L \in \mathbb{R}^D$ with density $p(\mathbf{x}^L)$. The goal of forward UQ is to estimate $p(\mathbf{x}^H)$. With a random input vector $\boldsymbol{\xi} \in \mathbb{R}^M$ and its density $p(\boldsymbol{\xi})$, the widely adopted surrogate approach seeks to approximate the density $p(\mathbf{x}^H|\boldsymbol{\xi})$ and estimate $p(\mathbf{x}^H)$ as

$$p(\mathbf{x}^H) = \int_{\mathbb{R}^M} p(\mathbf{x}^H|\boldsymbol{\xi})p(\boldsymbol{\xi})d\boldsymbol{\xi},$$

but suffers from two major issues, which are the high complexity of building the surrogate model when the dimension of $\boldsymbol{\xi}$ is high and the expensive cost of collecting HF QoI realizations. To alleviate the first issue, bi-fidelity approaches usually introduce an LF density $p(\mathbf{x}^L)$, approximate $p(\mathbf{x}^H|\mathbf{x}^L)$ instead of $p(\mathbf{x}^H|\boldsymbol{\xi})$, and marginalize the random input vector

$\boldsymbol{\xi}$ to eliminate the effect of its high-dimensionality,

$$\begin{aligned}
p(\mathbf{x}^H) &= \int_{\mathbb{R}^D} \int_{\mathbb{R}^M} p(\mathbf{x}^H, \mathbf{x}^L, \boldsymbol{\xi}) d\boldsymbol{\xi} d\mathbf{x}^L && \text{introduce LF model} \\
&= \int_{\mathbb{R}^D} \int_{\mathbb{R}^M} p(\mathbf{x}^H, \boldsymbol{\xi} | \mathbf{x}^L) p(\mathbf{x}^L) d\boldsymbol{\xi} d\mathbf{x}^L && \text{condition on LF model} \\
&= \int_{\mathbb{R}^D} p(\mathbf{x}^H | \mathbf{x}^L) p(\mathbf{x}^L) d\mathbf{x}^L. && \text{marginalization}
\end{aligned}$$

For the second issue, ROMs introduce a low-dimensional latent random vector $\mathbf{z} \in \mathbb{R}^d$ with $d \ll D$ to establish a connection between the LF and HF models $p(\mathbf{x}^H | \mathbf{x}^L)$,

$$\begin{aligned}
p(\mathbf{x}^H) &= \int_{\mathbb{R}^D} p(\mathbf{x}^H | \mathbf{x}^L) p(\mathbf{x}^L) d\mathbf{x}^L \\
&= \int_{\mathbb{R}^D} \int_{\mathbb{R}^d} p(\mathbf{x}^H | \mathbf{z}, \mathbf{x}^L) p(\mathbf{z} | \mathbf{x}^L) p(\mathbf{x}^L) d\mathbf{z} d\mathbf{x}^L.
\end{aligned}$$

The latent variable \mathbf{z} determines a low-dimensional manifold that captures the relationship between the LF and HF QoI, significantly reducing the required HF data for training.

In this work, we assume the Markov property holds, meaning $p(\mathbf{x}^H | \mathbf{z}, \mathbf{x}^L) = p(\mathbf{x}^H | \mathbf{z})$, which produces an auto-encoder structure as

$$p(\mathbf{x}^H) = \int_{\mathbb{R}^D} \int_{\mathbb{R}^d} \underbrace{p(\mathbf{x}^H | \mathbf{z})}_{\text{decoder}} \underbrace{p(\mathbf{z} | \mathbf{x}^L)}_{\text{encoder}} p(\mathbf{x}^L) d\mathbf{z} d\mathbf{x}^L.$$

After the auto-encoder structure is built, HF QoI can be estimated as

$$p(\mathbf{x}^H) = \int_{\mathbb{R}^d} p(\mathbf{x}^H | \mathbf{z}) p(\mathbf{z}) d\mathbf{z}.$$

A similar idea of Bayesian multi-fidelity modeling is expressed in [32]. This pipeline consists of three key components, namely, an encoder $p(\mathbf{z} | \mathbf{x}^L)$, the latent density $p(\mathbf{z})$, and a decoder $p(\mathbf{x}^H | \mathbf{z})$. In this section, we discuss two models to construct these three components. In Section 2.1, we introduce a VAE approach to build the encoder and the decoder in a Bayesian probabilistic manner. In Section 2.2, we discuss the design of the latent variable \mathbf{z} with its underlying motivation.

2.1. Variational Autoencoder

This section introduces the VAE approach [22, 23], which is a prevalent deep generative model capable of estimating an unknown density $p(\mathbf{x})$ from samples of \mathbf{x} and performing efficient synthesis of new data. As a deep Bayesian model, VAE compresses and reconstructs data in a non-linear and probabilistic manner, while regularizing the model via a KL divergence term, as in Equation (2.2), which distinguishes it from regular AE models. The VAE is composed of two distinct probabilistic components, namely the encoder and the decoder; see Figure 2. In contrast to AEs, the probabilistic encoder and decoder of a VAE map the input data to random vectors, rather than deterministic values. The probabilistic encoder

produces two separate vectors, representing the mean and standard deviation of a resulting multivariate Gaussian random vector in the latent space. In this context, the covariance matrix of the resulting multivariate Gaussian is assumed to be diagonal. The probabilistic decoder maps latent variables back to the observation space by sampling the resulting decoder output distribution. When the expected output is continuous, which is the primary focus of this work, the decoder result is traditionally assumed to be deterministic and returns the mean value of the decoder distribution [22]. In other words, the decoder $p(\mathbf{x}|\mathbf{z})$ becomes a Dirac distribution located at $D(\mathbf{z})$, where D is the deterministic decoder function. By enforcing a prior on the latent variable \mathbf{z} , the VAE can synthesize new samples of \mathbf{x} by sampling the latent variable and evaluating it through the decoder.

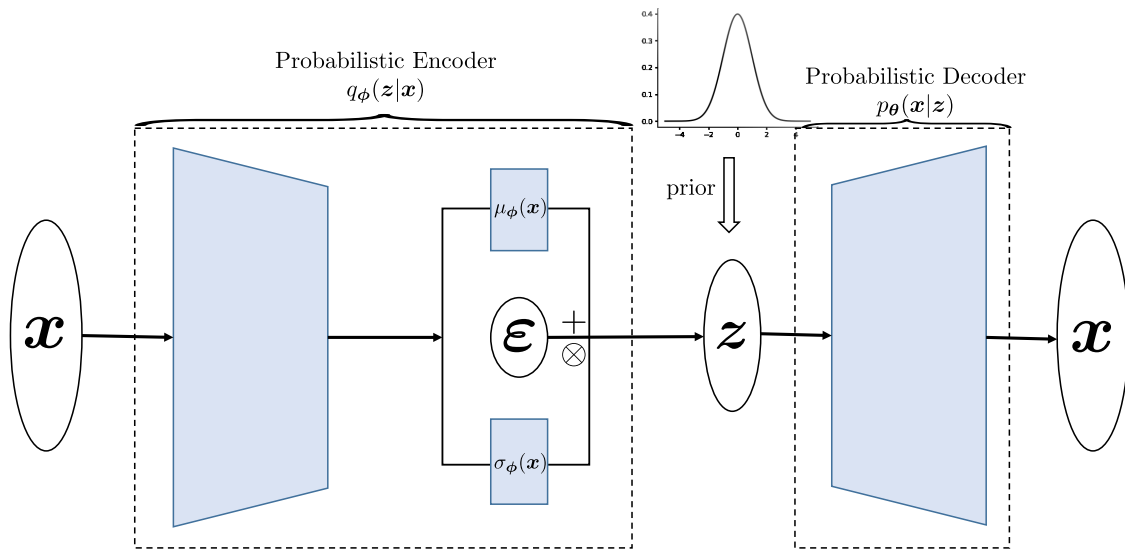


Figure 2: The probabilistic encoder $q_\phi(\mathbf{z}|\mathbf{x})$ of a VAE produces two separate vectors, $\boldsymbol{\mu}_\phi(\mathbf{x})$ and $\boldsymbol{\sigma}_\phi(\mathbf{x})$, which represent the mean and standard deviation of a resulting latent variable \mathbf{z} following a multivariate Gaussian distribution. The random vector $\boldsymbol{\varepsilon} \sim \mathcal{N}(\mathbf{0}, \mathbf{I})$ provides randomness for the encoder output \mathbf{z} and is used for the reparameterization trick in Equation (2.3). White circles are random vectors and blue blocks are parameterized neural networks.

In detail, VAE introduces a latent variable \mathbf{z} with its prior $p(\mathbf{z})$ in a low-dimensional latent space and parameterizes a probabilistic decoder $p_\theta(\mathbf{x}|\mathbf{z})$ with parameters $\boldsymbol{\theta}$ to establish a joint density $p_\theta(\mathbf{x}, \mathbf{z})$. According to Bayes' rule, the posterior density is

$$p_\theta(\mathbf{z}|\mathbf{x}) = \frac{p(\mathbf{z})p_\theta(\mathbf{x}|\mathbf{z})}{\int p_\theta(\mathbf{x}, \mathbf{z})d\mathbf{z}}.$$

This $p_\theta(\mathbf{z}|\mathbf{x})$ is intractable to compute due to the unknown marginal density $\int p_\theta(\mathbf{x}, \mathbf{z})d\mathbf{z}$. To address this issue, VAE employs a variational inference approach [33] and approximates

the posterior with a parameterized density $q_\phi(\mathbf{z}|\mathbf{x})$ with parameters ϕ . By introducing the variational replacement q_ϕ , the log-likelihood of \mathbf{x} can be decomposed as

$$\log(p_\theta(\mathbf{x})) = \underbrace{\text{KL}(q_\phi(\mathbf{z}|\mathbf{x})||p_\theta(\mathbf{z}|\mathbf{x}))}_{\text{ELBO}} + \mathbb{E}_{q_\phi} \log\left(\frac{p_\theta(\mathbf{x}, \mathbf{z})}{q_\phi(\mathbf{z}|\mathbf{x})}\right), \quad (2.1)$$

where $\text{KL}(\cdot||\cdot)$ is the Kullback-Leibler (KL) divergence and \mathbb{E}_{q_ϕ} is the expectation over $q_\phi(\mathbf{z}|\mathbf{x})$. The KL divergence term in Equation (2.1) measures the discrepancy between the true posterior $p_\theta(\mathbf{z}|\mathbf{x})$ and the variational posterior $q_\phi(\mathbf{z}|\mathbf{x})$ and is unknown in practice. The second term in Equation (2.1) is known as evidence lower bound (ELBO), which is a lower bound of the log-likelihood due to the non-negativity of KL divergence. In variational inference, ELBO is maximized instead of the log-likelihood due to its tractable form. By maximizing ELBO, the VAE model enhances a lower bound value of the log-likelihood and mitigates the discrepancy between the variational and true posteriors.

The VAE objective function, ELBO, can be further decomposed into two parts

$$\begin{aligned} \text{ELBO}(\phi, \theta) &= \mathbb{E}_{q_\phi} \log\left(\frac{p_\theta(\mathbf{x}, \mathbf{z})}{q_\phi(\mathbf{z}|\mathbf{x})}\right) \\ &= \underbrace{-\text{KL}(q_\phi(\mathbf{z}|\mathbf{x})||p(\mathbf{z}))}_{\text{regularization term}} + \underbrace{\mathbb{E}_{q_\phi} \log(p_\theta(\mathbf{x}|\mathbf{z}))}_{\text{reconstruction term}}. \end{aligned} \quad (2.2)$$

Note that ELBO also depends on \mathbf{x} but gets omitted here. The first part is the KL divergence between the prior $p(\mathbf{z})$ and the variational posterior $q_\phi(\mathbf{z}|\mathbf{x})$, which functions as a regularization term for the probabilistic encoder by enforcing the encoder outputs close to $p(\mathbf{z})$. The second term, $\mathbb{E}_{q_\phi} \log(p_\theta(\mathbf{x}|\mathbf{z}))$, is the conditional log-likelihood of \mathbf{x} that is averaged on the variational posterior, $\mathbf{z} \sim q_\phi$. This component is often perceived as a negative reconstruction error. For example, when the conditional density $p_\theta(\mathbf{x}|\mathbf{z})$ is Gaussian centered at the decoder output $D_\theta(\mathbf{z})$, where $D_\theta(\mathbf{z})$ is a neural-network-based decoder function, $\log(p_\theta(\mathbf{x}|\mathbf{z}))$ becomes the negative 2-norm reconstruction error $-\|\mathbf{x} - D_\theta(\mathbf{z})\|^2$.

In order to estimate θ and ϕ , gradient ascent is applied to maximize ELBO with gradient $\nabla_\phi \text{ELBO}$ and $\nabla_\theta \text{ELBO}$. However, the gradient of ELBO with respect to ϕ , i.e.,

$$\nabla_\phi \text{ELBO} = \nabla_\phi \mathbb{E}_{q_\phi} \log\left(\frac{p_\theta(\mathbf{x}, \mathbf{z})}{q_\phi(\mathbf{z}|\mathbf{x})}\right)$$

cannot be computed directly since the expectation \mathbb{E}_{q_ϕ} depends on ϕ . To mitigate this issue, VAE uses a new random vector $\boldsymbol{\varepsilon} \sim \mathcal{N}(0, \mathbf{I})$ and represents latent samples as $\mathbf{z}_\boldsymbol{\varepsilon} = \boldsymbol{\sigma}_\phi(\mathbf{x}) \otimes \boldsymbol{\varepsilon} + \boldsymbol{\mu}_\phi(\mathbf{x})$, where \otimes is Hadamard (element-wise) product. Stochastic gradient ascent (or its variants) is performed for each mini-batch of samples $\{\mathbf{x}_i\}_{i=1}^B$ by passing them through the encoder and obtaining $\boldsymbol{\sigma}_\phi(\mathbf{x}_i)$ and $\boldsymbol{\mu}_\phi(\mathbf{x}_i)$ and generating new $\mathbf{z}_{\boldsymbol{\varepsilon}_i}$ by sampling $\boldsymbol{\varepsilon}_i$. An

unbiased estimator of the gradient is evaluated as

$$\begin{aligned}
\nabla_{\phi} \text{ELBO} &= \nabla_{\phi} \mathbb{E}_{\varepsilon} \log \left(\frac{p_{\theta}(\mathbf{x} | \mathbf{z}_{\varepsilon}) p(\mathbf{z}_{\varepsilon})}{q_{\phi}(\mathbf{z}_{\varepsilon} | \mathbf{x})} \right) \\
&= \mathbb{E}_{\varepsilon} \nabla_{\phi} \log \left(\frac{p_{\theta}(\mathbf{x} | \mathbf{z}_{\varepsilon}) p(\mathbf{z}_{\varepsilon})}{q_{\phi}(\mathbf{z}_{\varepsilon} | \mathbf{x})} \right) \\
&\approx \frac{1}{B} \sum_{i=1}^B \nabla_{\phi} \log \left(\frac{p_{\theta}(\mathbf{x} = \mathbf{x}_i | \mathbf{z} = \mathbf{z}_{\varepsilon_i}) p(\mathbf{z} = \mathbf{z}_{\varepsilon_i})}{q_{\phi}(\mathbf{z} = \mathbf{z}_{\varepsilon_i} | \mathbf{x} = \mathbf{x}_i)} \right).
\end{aligned} \tag{2.3}$$

The method for estimating the gradient in Equation (2.3), known as the reparametrization trick [22], can be applied to any form of $q_{\phi}(\mathbf{z} | \mathbf{x})$, provided that it is associated with an easy-to-sample distribution. It allows for decoupling of the expectation from ϕ in Equation (2.3), thereby enabling the optimization of the objective function.

2.2. Auto-regressive Method

The central challenge of bi-fidelity modeling is to establish a connection between LF and HF model outputs. The VAE in Section 2.1 provides a solution for building the encoder and decoder for searching an appropriate latent space, while we also need a suitable architecture for the latent variable \mathbf{z} to model the relation between LF and HF solutions. This architecture should be relatively simple due to the scarcity of HF training data. For example, in [34], the authors use an encoder-decoder structure in conjunction with a latent bi-fidelity modeling approach that minimizes the distance between reduced basis coefficients. We extend this method to a more generalized form.

For the case of the probabilistic encoder and decoder, we split the latent random vector \mathbf{z} into two parts, \mathbf{z}^L and \mathbf{z}^H , and apply a linear auto-regression from \mathbf{z}^L to \mathbf{z}^H , inspired by the well-known Gaussian process (GP) based linear auto-regressive method [35, 36, 37]. This approach incorporates multivariate Gaussian priors for both fidelity models and postulates a linear, element-wise relationship between the models. The HF latent random vector \mathbf{z}^H can be represented as a transformation of the LF latent random vector \mathbf{z}^L through

$$z_i^H = a_i z_i^L + b_i, \forall i = 1, 2, \dots, d$$

where a_i serves as a scaling factor and b_i is a Gaussian random variable. In some works [36, 35] z_i^H and z_i^L are indexed with a spatial variable, which has been omitted here for clarity. The model assumes that no knowledge of z_i^H can be extracted from z_j^L if z_i^L is known and $i \neq j$, which implies $\text{Cov}(z_i^H, z_j^L | z_i^L) = 0, \forall i \neq j$.

3. Bi-fidelity Variational Auto-encoder

In this section, we present the BF-VAE model. Section 3.1 outlines the architecture of the BF-VAE, a bi-fidelity extension of the ELBO objective function, and an algorithm designed for training BF-VAE. The bi-fidelity information bottleneck (BF-IB) theory is introduced in Section 3.2, providing an insightful interpretation of BF-VAE from the perspective of information theory. Section 3.3 delves into the analysis of an error stemming from the probabilistic encoder trained by LF data.

3.1. Architecture, Objective Functions, and Algorithm

The principle behind the BF-VAE involves maximizing a lower bound of the HF log-likelihood, as VAE does, but primarily utilizing LF data. To achieve this, a VAE-based structure is devised to leverage a latent space to model the relationship between the LF and HF data. The BF-VAE model is comprised of three probabilistic components: an encoder, a latent auto-regression, and a decoder. The probabilistic encoder $q_\phi(\mathbf{z}^L|\mathbf{x}^L)$, parameterized with ϕ and trained using LF data, maps LF observations into LF latent representations. The latent auto-regression $p_\psi(\mathbf{z}^H|\mathbf{z}^L)$, parameterized with ψ and specifically designed for a bi-fidelity regression in the latent space, as shown in Equation (3.1), significantly reduces the amount of HF data required for training due to its low-dimensionality. The probabilistic decoder $p_\theta(\mathbf{x}^H|\mathbf{z}^H)$, parameterized with θ , is first pre-trained with LF data and then refined with HF data, mapping the HF latent representations back into the observation space by returning the mean of the resulting HF distribution. A schematic illustration of the proposed BF-VAE model is depicted in Figure 3.

The particularly crucial part of BF-VAE is building a connection from LF latent variable \mathbf{z}^L to HF latent variable \mathbf{z}^H . As presented in Section 2.2, we specify the latent conditional density $p_\psi(\mathbf{z}^H|\mathbf{z}^L)$ to be a linear auto-regressive model and assume it as $\mathcal{N}(\mathbf{K}_\psi(\mathbf{z}^L), \gamma^2\mathbf{I})$ with parameters ψ . The mapping \mathbf{K}_ψ consists of two parameterized vector components, \mathbf{a}_ψ and \mathbf{b}_ψ , and is defined by the affine transformation

$$\mathbf{K}_\psi(\mathbf{z}^L) = \mathbf{a}_\psi \otimes \mathbf{z}^L + \mathbf{b}_\psi. \quad (3.1)$$

The mapping \mathbf{K}_ψ is implemented as a simplified single-layer neural network with a diagonal weight matrix and a bias vector. The hyperparameter γ is fixed for all entries for simplicity. When $\gamma \rightarrow 0$, $p_\psi(\mathbf{z}^H|\mathbf{z}^L)$ converges in distribution to the Dirac distribution $\delta_{\mathbf{K}_\psi(\mathbf{z}^L)}$, which makes the latent auto-regression a deterministic map. The hyperparameter γ represents our confidence on how accurately \mathbf{K}_ψ captures the relation between the LF and HF latent variables; see more discussion about γ in Section 4.2.

The objective function of the BF-VAE is a variational lower bound of HF log-likelihood as follows

$$\begin{aligned} \log p_{\theta, \psi}(\mathbf{x}^H) &= \text{KL}\left(q_\phi(\mathbf{z}_\psi|\mathbf{x}^L) \parallel p_\theta(\mathbf{z}_\psi|\mathbf{x}^H)\right) + \mathbb{E}_{q_\phi(\mathbf{z}_\psi|\mathbf{x}^L)} \left[\log \left(\frac{p_\theta(\mathbf{x}^H, \mathbf{z}_\psi)}{q_\phi(\mathbf{z}_\psi|\mathbf{x}^L)} \right) \right] \\ &\geq \mathbb{E}_{q_\phi(\mathbf{z}_\psi|\mathbf{x}^L)} \left[\log \left(\frac{p_\theta(\mathbf{x}^H, \mathbf{z}_\psi)}{q_\phi(\mathbf{z}_\psi|\mathbf{x}^L)} \right) \right] = \text{ELBO}^{\text{BF}}(\phi, \psi, \theta), \end{aligned} \quad (3.2)$$

where the density of $\mathbf{z}_\psi := (\mathbf{z}^L, \mathbf{z}^H)$ is determined by the latent conditional density $p_\psi(\mathbf{z}^H|\mathbf{z}^L)$ and the prior $p(\mathbf{z}^L)$. The inequality above follows from the non-negativity property of KL divergence. The lower bound of HF log-likelihood in Equation (3.2) is called bi-fidelity ELBO (BF-ELBO), and denoted as $\text{ELBO}^{\text{BF}}(\phi, \psi, \theta)$. The BF-ELBO consists of two terms,

$$\text{ELBO}^{\text{BF}}(\phi, \psi, \theta) = \underbrace{-\text{KL}\left(q_\phi(\mathbf{z}^L|\mathbf{x}^L) \parallel p(\mathbf{z}^L)\right)}_{\text{regularization term}} + \underbrace{\mathbb{E}_{q_\phi(\mathbf{z}_\psi|\mathbf{x}^L)} \left[\log p_\theta(\mathbf{x}^H|\mathbf{z}_\psi) \right]}_{\text{HF reconstruction term}}. \quad (3.3)$$

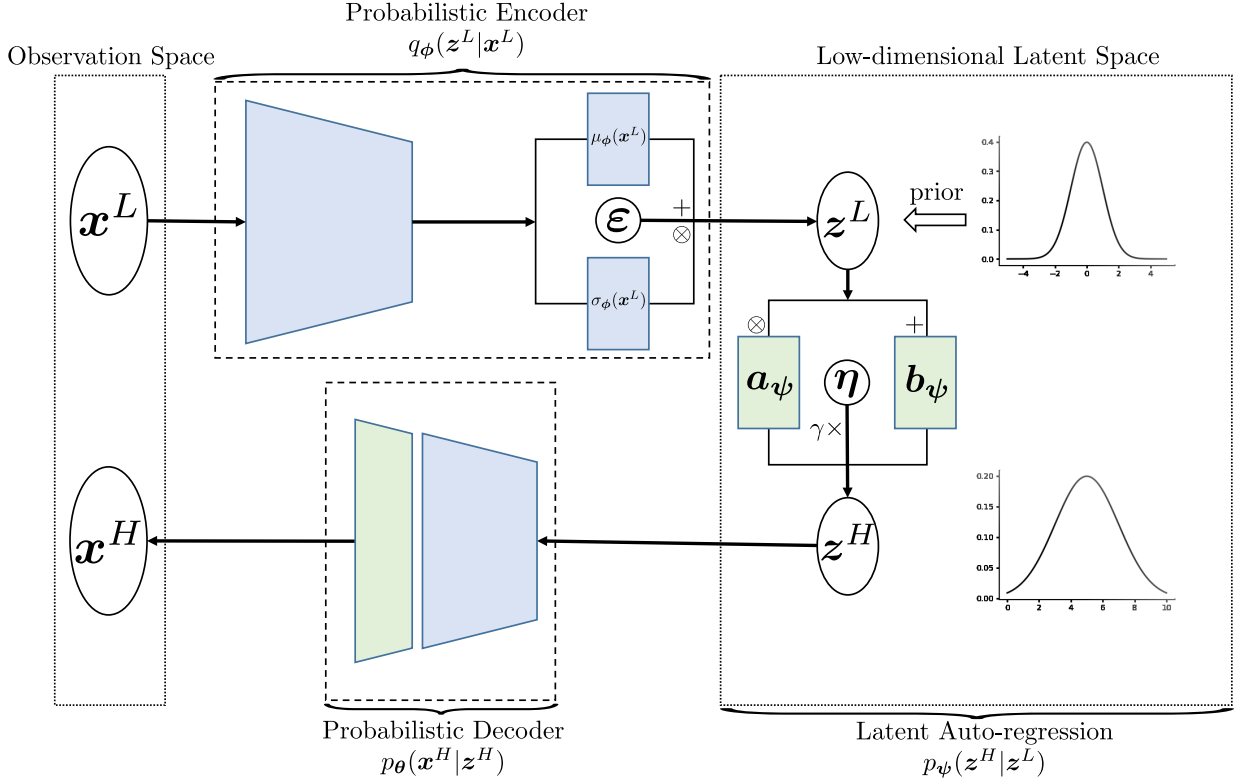


Figure 3: Structure of the proposed BF-VAE model. The probabilistic encoder $q_\phi(\mathbf{z}^L|\mathbf{x}^L)$ produces two independent vectors, $\mu_\phi(\mathbf{x}^L)$ and $\sigma_\phi(\mathbf{x}^L)$, which represent the mean and standard deviation of a resulting multivariate Gaussian. The latent auto-regression $p_\psi(\mathbf{z}^H|\mathbf{z}^L)$ is a simplified single-layer neural network \mathbf{K}_ψ defined in Equation (3.1) added with a noise $\gamma\boldsymbol{\eta}$. The probabilistic decoder $p_\theta(\mathbf{x}^H|\mathbf{z}^H)$ is pre-trained by LF data via the transfer learning technique, with its last layer tuned by LF and HF data pairs. White circles are random vectors and colored blocks are parameterized components for training. Blue blocks are solely trained by LF data and green blocks are trained by both LF and HF data.

The first term regularizes the encoder training by enforcing the encoder output close to the prior $p(\mathbf{z}^L)$. The second term is the HF log-likelihood conditioned on the latent variable \mathbf{z}_ψ and perceived as an HF reconstruction term. For example, when $p_\theta(\mathbf{x}^H|\mathbf{z}_\psi)$ is a Gaussian center at the decoder output $D_\theta(\mathbf{z}^H)$ with covariance $\beta\mathbf{I}$, the HF reconstruction term is a negative 2-norm $-\beta^{-1}\|\mathbf{x}^H - D_\theta(\mathbf{z}^H)\|^2$ with \mathbf{z}^H drawn from the encoder and the latent auto-regression with input \mathbf{x}^L . Note that by the Markov property $p(\mathbf{x}^H|\mathbf{z}_\psi)$ is equivalent to $p(\mathbf{x}^H|\mathbf{z}^H)$. We use \mathbf{z}_ψ as the conditional variable for $p_\theta(\mathbf{x}^H|\mathbf{z}_\psi)$ so that it is consistent with the expectation $\mathbb{E}_{q_\phi(\mathbf{z}_\psi|\mathbf{x}^L)}$. A detailed derivation of Equations (3.2) and (3.3) are presented in Appendix A.

Optimizing BF-ELBO requires a large amount of both LF and HF data from their joint

distribution $p(\mathbf{x}^L, \mathbf{x}^H)$ for convergence. However, the scarcity of HF data presents a challenge under the bi-fidelity setting. To address this issue, we apply a transfer learning technique, in which we opt to train the encoder and decoder using a large set of LF data, considering that the parameter spaces of ϕ and θ are significantly larger than that of ψ . The small parameter space of ψ as a single layer in the low-dimensional latent space allows it to be trained solely with pairs of LF and HF data. As a result, we optimize the BF-ELBO in two steps, with two separate objectives,

$$\text{ELBO}^{\text{LF}}(\phi, \theta) = -\text{KL}(q_\phi(\mathbf{z}^L|\mathbf{x}^L)||p(\mathbf{z}^L)) + \mathbb{E}_{q_\phi(\mathbf{z}^L|\mathbf{x}^L)}[\log(p_\theta(\mathbf{x}^L|\mathbf{z}^L))], \quad (3.4)$$

$$\text{ELBO}^{\text{HF}}(\psi, \theta) = \mathbb{E}_{q_{\phi^{L^*}}(\mathbf{z}_\psi|\mathbf{x}^L)}[\log p_\theta(\mathbf{x}^H|\mathbf{z}_\psi)], \quad (3.5)$$

where ϕ^{L^*} in ELBO^{HF} is the optimal ϕ for maximizing ELBO^{LF} . The first objective function $\text{ELBO}^{\text{LF}}(\phi, \theta)$ is equivalent to a regular ELBO function discussed in Equation (2.2), as it trains a low-fidelity VAE (LF-VAE) solely using LF data. Trained LF-VAE returns the optimal LF encoder parameters ϕ^{L^*} and LF decoder parameters θ^{L^*} . We assume the optimal HF decoder parameters θ^{H^*} is close to θ^{L^*} in the parameter space. Furthermore, we fix the decoder’s parameters except for the last layer and set θ^{L^*} as the initial value for further optimizing ELBO^{HF} using both LF and HF data to obtain optimal HF parameters ψ^{H^*}, θ^{H^*} . Note that θ^{H^*} and θ^{L^*} share most parameters except the decoder’s last layer due to this transfer learning technique.

The presence of the parameter ψ in the expectation term in Equation (3.5) poses a challenge for the estimation of the gradients with respect to ψ . To address it, we leverage the reparameterization trick outlined in Equation (2.3). Specifically, we introduce an auxiliary vector $\boldsymbol{\eta} \sim \mathcal{N}(\mathbf{0}, \mathbf{I})$ and set

$$\mathbf{z}_\eta^H = \gamma\boldsymbol{\eta} + \mathbf{K}_\psi(\mathbf{z}^L). \quad (3.6)$$

With mini-batch bi-fidelity samples $\{\mathbf{x}_i^L, \mathbf{x}_i^H\}_{i=1}^B$, the gradient w.r.t. ψ is estimated as

$$\begin{aligned} \nabla_\psi \text{ELBO}^{\text{HF}}(\psi, \theta) &= \mathbb{E}_{p_{\phi^{L^*}}(\mathbf{z}^L|\mathbf{x}^L)}[\nabla_\psi \mathbb{E}_{p_\psi(\mathbf{z}^H|\mathbf{z}^L)}[\log p_\theta(\mathbf{x}^H|\mathbf{z}^H)]] \\ &= \mathbb{E}_{p_{\phi^{L^*}}(\mathbf{z}^L|\mathbf{x}^L)}[\mathbb{E}_\eta[\nabla_\psi \log p_\theta(\mathbf{x}^H|\mathbf{z}_\eta^H)]] \\ &\approx \frac{1}{B} \sum_{i=1}^B \nabla_\psi \log p_\theta(\mathbf{x}^H = \mathbf{x}_i^H | \mathbf{z}^H = \mathbf{z}_{\boldsymbol{\eta}_i}^H), \end{aligned}$$

where B is batch size and $\mathbf{z}_{\boldsymbol{\eta}_i}^H$ is the i -th sample from \mathbf{x}_i^L and $\boldsymbol{\eta}_i$ as shown in Equation (3.6). With the estimated gradients, we maximize $\text{ELBO}^{\text{LF}}(\phi, \theta)$ and $\text{ELBO}^{\text{HF}}(\psi, \theta)$ via stochastic gradient ascent (or its variants). To synthesize HF QoI samples, we sample from $p(\mathbf{z}^L)$ and subsequently propagate the samples through the trained latent auto-regressor with parameters ψ^{H^*} and decoder with parameters θ^{H^*} . A summary of the steps in BF-VAE is provided in Algorithm 1.

Algorithm 1: Bi-Fidelity Variational Auto-Encoder (BF-VAE)

Input: LF training set $\{\tilde{\mathbf{x}}_i^L\}_{i=1}^N$, LF-HF joint training set $\{(\mathbf{x}_i^L, \mathbf{x}_i^H)\}_{i=1}^n$

Output: Parameters $\boldsymbol{\psi}^{H*}, \boldsymbol{\theta}^{H*}$ for a HF density $p_{\boldsymbol{\theta}, \boldsymbol{\psi}}(\mathbf{x}^H)$

- 1: Train a LF VAE by maximizing $\text{ELBO}^{\text{LF}}(\boldsymbol{\phi}, \boldsymbol{\theta})$ in Equation (3.4) with LF realizations $\{\tilde{\mathbf{x}}_i^L\}_{i=1}^N$ to attain maximizers $\boldsymbol{\phi}^{L*}, \boldsymbol{\theta}^{L*} = \text{argmax}_{\boldsymbol{\phi}, \boldsymbol{\theta}} \text{ELBO}^{\text{LF}}(\boldsymbol{\phi}, \boldsymbol{\theta})$.
 - 2: Build a BF-VAE as shown in Figure 3 with parameters of the encoder and the decoder assigned to be $\boldsymbol{\phi}^{L*}, \boldsymbol{\theta}^{L*}$, and the latent auto-regression map $\mathbf{K}_{\boldsymbol{\psi}}(\cdot)$ in Equation (3.1) being initialized as an identity map.
 - 3: Fix all the parameters of the BF-VAE except the decoder’s last layer and the latent auto-regression’s parameters.
 - 4: Train the BF-VAE by maximizing $\text{ELBO}^{\text{HF}}(\boldsymbol{\psi}, \boldsymbol{\theta})$ in Equation (3.5) with sample pairs $\{(\mathbf{x}_i^L, \mathbf{x}_i^H)\}_{i=1}^n$ and find maximizers $\boldsymbol{\psi}^{H*}, \boldsymbol{\theta}^{H*} = \text{argmax}_{\boldsymbol{\psi}, \boldsymbol{\theta}} \text{ELBO}^{\text{HF}}(\boldsymbol{\psi}, \boldsymbol{\theta})$.
-

3.2. Bi-fidelity Information Bottleneck

One of the core ideas of bi-fidelity modeling is to fully exploit information from LF data for building HF results with limited HF data. However, to the best of the authors’ knowledge, there is no previous work that explicitly models the bi-fidelity information transfer process incorporating information theory. In this work, we apply the information bottleneck (IB) principle [31, 38] to the BF-VAE model. The IB principle aims to define the essence of a “good” latent representation of data by finding a balance between preservation and compression in the sense of information. According to IB, an optimal latent representation of given data is maximally informative about the output while simultaneously compressive with respect to a given input.

In this section, we propose an interpretation of the BF-VAE model through the lens of the bi-fidelity IB (BF-IB) theory. We show that maximizing ELBO^{BF} in Equation (3.3) is equivalent to maximizing the BF-IB objective function in Equation (3.7) with $\beta = 1$ using $(\mathbf{x}^L, \mathbf{x}^H)$ data, which discloses the fact that training a BF-VAE model is a bi-fidelity information transferring process. Our analysis in this section builds a bridge between information theory and log-likelihood maximization in the bi-fidelity setting and presents a novel information-theoretic perspective on the BF-VAE model.

The mutual information, which is a non-negative, symmetric function, reflects the quantity of information that can be obtained about one random vector by observing another random vector. The definition of mutual information is as follows.

Definition 3.1. The mutual information [39] between random vectors \mathbf{x} and \mathbf{y} is

$$\mathbb{I}(\mathbf{x}, \mathbf{y}) := \text{KL}(p(\mathbf{x}, \mathbf{y}) \| p(\mathbf{x})p(\mathbf{y})) = \mathbb{E}_{p(\mathbf{x}, \mathbf{y})} \log \left(\frac{p(\mathbf{x}, \mathbf{y})}{p(\mathbf{x})p(\mathbf{y})} \right),$$

where $p(\mathbf{x}, \mathbf{y})$ is the joint distribution of \mathbf{x} and \mathbf{y} .

For our bi-fidelity case, our goal is to find a latent representative random vector $\mathbf{z}_{\boldsymbol{\psi}}$ corresponding to \mathbf{x}^L for re-building HF QoI \mathbf{x}^H . According to the formula (15) in [31] or

formula (5.164) in [40], the bi-fidelity information bottleneck (BF-IB) objective function that we will maximize is

$$\text{IB}_{\beta}^{\text{BF}}(\phi, \psi, \theta) := \mathbb{I}(\mathbf{z}_{\psi}, \mathbf{x}^H) - \beta \mathbb{I}(\mathbf{x}^L, \mathbf{z}_{\psi}), \quad (3.7)$$

where β is a non-negative hyperparameter, and ϕ, θ are parameters of the encoder and decoder, respectively. The first term $\mathbb{I}(\mathbf{z}_{\psi}, \mathbf{x}^H)$ represents the preserved information from \mathbf{z}_{ψ} to \mathbf{x}^H by the decoder, while the second term $\mathbb{I}(\mathbf{x}^L, \mathbf{z}_{\psi})$ represents the information compressed by the encoder. The hyperparameter β is adjusted to balance the tradeoff between the information compression and the preservation. By maximizing the BF-IB objective function, we aim to find an optimal latent random vector \mathbf{z}_{ψ} as well as its relation with $\mathbf{x}^L, \mathbf{x}^H$, which are parameterized by ψ, ϕ , and θ . Note that when the mutual information between \mathbf{x}^L and \mathbf{x}^H is zero, which means LF and HF data are independent, the optimization of the IB-BF function is vacuous. The schematic in Figure 4 describes the concept of BF-IB.

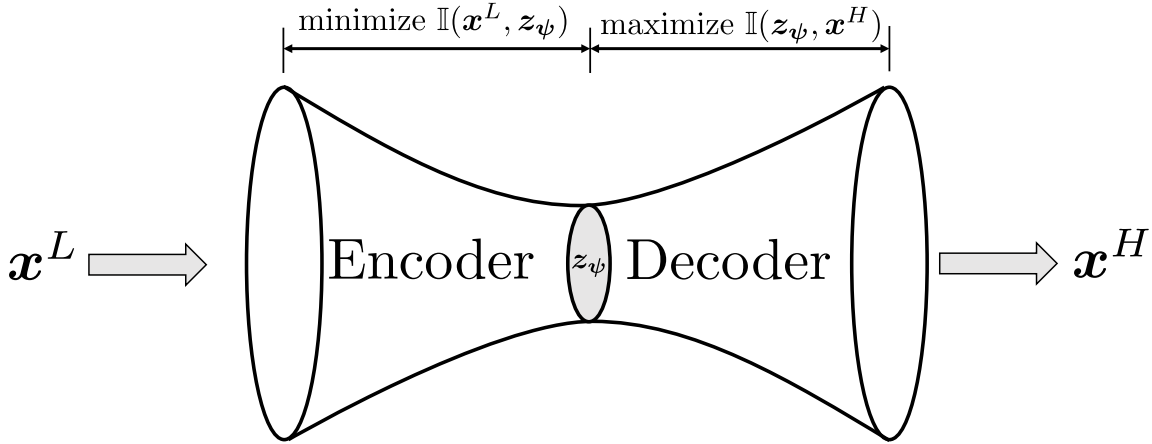


Figure 4: The bi-fidelity information bottleneck architecture has an encoder and a decoder, impacted by the information compression function $\mathbb{I}(\mathbf{x}^L, \mathbf{z}_{\psi})$ and information preservation function $\mathbb{I}(\mathbf{z}_{\psi}, \mathbf{x}^H)$, respectively. The random vector \mathbf{z}_{ψ} is designed to disclose the relation between LF and HF data in the latent space. The bottleneck part is necessary since only a limited number of HF samples are available for learning the relationship between LF and HF data.

The BF-IB objective function can be decomposed as follows,

$$\text{IB}_{\beta}^{\text{BF}}(\phi, \psi, \theta) \equiv \mathbb{E}_{p(\mathbf{x}^L, \mathbf{x}^H)} \left[\mathbb{E}_{q_{\phi}(\mathbf{z}_{\psi} | \mathbf{x}^L)} \left[\log p_{\theta}(\mathbf{x}^H | \mathbf{z}_{\psi}) \right] - \beta \text{KL}(q_{\phi}(\mathbf{z}^L | \mathbf{x}^L) \| p(\mathbf{z}^L)) \right]. \quad (3.8)$$

When $\beta = 1$, BF-IB objective function becomes

$$\begin{aligned} \text{IB}_{\beta=1}^{\text{BF}}(\phi, \psi, \theta) &\equiv \mathbb{E}_{p(\mathbf{x}^L, \mathbf{x}^H)} \left[\mathbb{E}_{q_{\phi}(\mathbf{z}_{\psi} | \mathbf{x}^L)} \left[\log p_{\theta}(\mathbf{x}^H | \mathbf{z}_{\psi}) \right] - \text{KL}(q_{\phi}(\mathbf{z}^L | \mathbf{x}^L) \| p(\mathbf{z}^L)) \right] \\ &= \mathbb{E}_{p(\mathbf{x}^L, \mathbf{x}^H)} [\text{ELBO}^{\text{BF}}(\phi, \psi, \theta)] \end{aligned}$$

This proves that the BF-IB function with $\beta = 1$ is equivalent to BF-ELBO in Equation (3.3) averaged with respect to the true joint distribution $p(\mathbf{x}^L, \mathbf{x}^H)$. The proof of (3.8) is presented in Appendix B with Markov property assumed. In Section 4.2, we incorporate the hyperparameter β into a prior of the decoder density $p_{\theta}(\mathbf{x}^H|\mathbf{z}^H)$, yielding an equivalent objective function containing β . Because the BF-VAE Algorithm 1 approximately maximizes BF-ELBO using joint realizations from $p(\mathbf{x}^L, \mathbf{x}^H)$, it produces an output that not only maximizes a variational lower bound of the HF log-likelihood but also the IB-BF objective function.

3.3. Bi-fidelity Approximation Error

Similar to VAE in Section 2.1, the BF-VAE model introduces an encoder to approximate the posterior $p_{\theta}(\mathbf{z}_{\psi}|\mathbf{x}^H)$, which produces an approximation error stemming from its variational form. Moreover, since we employ LF data as the input of the encoder, the error also depends on the similarity between LF and HF data. In this section, we give the form of this error and provide insight into a measurement of similarity between LF and HF data under the current Bayesian framework.

Specifically, this error, denoted by \mathcal{E} , is the gap between HF log-likelihood and BF-ELBO averaging with respect to the true data distribution $p(\mathbf{x}^L, \mathbf{x}^H)$. The BF-VAE model assigns a family of multivariate Gaussian distribution q_{ϕ} to the encoder without any guarantee that the given family includes the true HF posterior. The error \mathcal{E} ,

$$\begin{aligned} \mathcal{E}(\boldsymbol{\psi}, \boldsymbol{\theta}) &:= \min_{\phi} \mathbb{E}_{p(\mathbf{x}^L, \mathbf{x}^H)} \left[\log p_{\theta, \psi}(\mathbf{x}^H) - \text{ELBO}^{BF}(\phi, \boldsymbol{\psi}, \boldsymbol{\theta}) \right] \\ &= \min_{\phi} \mathbb{E}_{p(\mathbf{x}^L, \mathbf{x}^H)} \left[\text{KL} \left(q_{\phi}(\mathbf{z}_{\psi}|\mathbf{x}^L) \parallel p_{\theta}(\mathbf{z}_{\psi}|\mathbf{x}^H) \right) \right], \end{aligned}$$

is directly derived from Equation (3.2). Since the error is a function of $\boldsymbol{\psi}$ and $\boldsymbol{\theta}$, the final performance of the trained BF-VAE model is determined by $\mathcal{E}(\boldsymbol{\psi}^{H*}, \boldsymbol{\theta}^{H*})$, where $\boldsymbol{\psi}^{H*}$ and $\boldsymbol{\theta}^{H*}$ are trained parameters. As a KL divergence average on bi-fidelity data $p(\mathbf{x}^L, \mathbf{x}^H)$, the error \mathcal{E} can be interpreted as the average difference between the latent representations from LF and HF, which depends on the similarity between LF and HF data.

To improve the BF-ELBO’s proximity to the HF log-likelihood, it is helpful to identify a form of $q_{\phi}(\mathbf{z}_{\psi}|\mathbf{x}^L)$ that is potentially close to $p_{\theta}(\mathbf{z}_{\psi}|\mathbf{x}^H)$. However, in practice, determining such a form is often infeasible [41]. Alternatively, bringing LF data closer to HF data can also reduce the error by making their latent representations more similar.

4. Priors and Hyperparameters

In the previous section, we introduced the principle concept of the BF-VAE model. In this section, we show two practical components of the BF-VAE model. We discuss the prior distribution selection in Section 4.1. An introduction to the hyperparameters and their effects on the BF-VAE performance is given in Section 4.2.

4.1. Choices of Prior Distributions

The selection of the prior distributions is a crucial aspect of Bayesian modeling, which are chosen to reflect our prior belief of the parameter or for computational feasibility. All the prior distributions utilized in the BF-VAE model are outlined in Table 1.

Table 1: Prior selection for different components of LF-VAE and BF-VAE is discussed in Section 3.1. Here, $\mu_\phi(\mathbf{x}^L)$ and $\sigma_\phi(\mathbf{x}^L)$ are the outputs of the variational encoder. \mathbf{K}_ψ is a parameterized latent mapping in Equation (3.1). $\{\gamma, \beta\}$ are hyperparameters.

Component	Notation	VAE Model(s)	Prior Distribution
LF Latent Variable	$p(\mathbf{z}^L)$	LF-VAE, BF-VAE	$\mathcal{N}(\mathbf{0}, \mathbf{I})$
Variational Encoder	$q_\phi(\mathbf{z}^L \mathbf{x}^L)$	LF-VAE, BF-VAE	$\mathcal{N}(\boldsymbol{\mu}_\phi(\mathbf{x}^L), \boldsymbol{\sigma}_\phi(\mathbf{x}^L))$
Latent Auto-regression	$p_\psi(\mathbf{z}^H \mathbf{z}^L)$	BF-VAE	$\mathcal{N}(\mathbf{K}_\psi(\mathbf{z}^L), \gamma^2 \mathbf{I})$
LF Decoder	$p_\theta(\mathbf{x}^L \mathbf{z}^L)$	LF-VAE	$\mathcal{N}(D_\theta(\mathbf{z}^L), \beta \mathbf{I})$
HF Decoder	$p_\theta(\mathbf{x}^H \mathbf{z}^H)$	BF-VAE	$\mathcal{N}(D_\theta(\mathbf{z}^H), \beta \mathbf{I})$

Let $\{\tilde{\mathbf{x}}_i^L\}_{i=1}^N \sim p(\mathbf{x}^L)$ and $\{\mathbf{x}_j^L, \mathbf{x}_j^H\}_{j=1}^n \sim p(\mathbf{x}^L, \mathbf{x}^H)$ denote the LF and BF training datasets, respectively. When using the priors in Table 1, the LF-ELBO in Equation (3.4) becomes

$$\begin{aligned} \text{ELBO}_{\beta}^{\text{LF}}(\phi, \theta) = & \underbrace{-\frac{1}{2} \left(\|\boldsymbol{\mu}_\phi(\tilde{\mathbf{x}}_i^L)\|_2^2 + \|\boldsymbol{\sigma}_\phi(\tilde{\mathbf{x}}_i^L)\|_2^2 - \mathbf{1}^T \log \boldsymbol{\sigma}_\phi^2(\tilde{\mathbf{x}}_i^L) \right)}_{\text{regularization}} \\ & + \frac{1}{N} \sum_{i=1}^N \left[\underbrace{\beta^{-1} \mathbb{E}_{q_\phi(\mathbf{z}^L|\mathbf{x}^L=\tilde{\mathbf{x}}_i^L)} \|D_\theta(\mathbf{z}^L) - \mathbf{x}_i^L\|_2^2}_{\text{LF reconstruction}} \right]. \end{aligned}$$

Similarly, the HF-ELBO in Equation (3.5) becomes

$$\text{ELBO}_{\beta}^{\text{HF}}(\psi, \theta) = \frac{1}{n} \sum_{i=1}^n \left[\underbrace{\beta^{-1} \mathbb{E}_{p_{\phi^*}(\mathbf{z}^L|\mathbf{x}^L=\mathbf{x}_i^L)} \left[\|D_\theta(\mathbf{z}^H) - \mathbf{x}_i^H\|_2^2 \right]}_{\text{BF reconstruction}} \right],$$

where $\mathbf{z}_{\eta_i}^H$ is computed as in Equation (3.6) with $\eta_i \sim \mathcal{N}(\mathbf{0}, \mathbf{I})$.

4.2. Hyperparameter Setting

The choice of hyperparameters is a key aspect in the encoding of prior knowledge for modeling. Specifically, BF-VAE consists of two primary hyperparameters, β in Equation (3.8) and Table 1 and γ in Equation (3.6), which must be specified before the training procedure.

Firstly, it is worth noting that $\text{ELBO}^{\text{BF}}(\phi, \psi, \theta)$ in Equation (3.3) with priors outlined in Table 1 is

$$\begin{aligned} \text{ELBO}^{\text{BF}}(\phi, \psi, \theta) = & -\text{KL}(q_\phi(\mathbf{z}^L|\mathbf{x}^L)\|p(\mathbf{z}^L)) + \beta^{-1} \mathbb{E}_{q_\phi(\mathbf{z}_\psi|\mathbf{x}^L)} \left[\|\mathbf{x}^H - D_\theta(\mathbf{z}^H)\|_2^2 \right] \\ \equiv & -\beta \text{KL}(q_\phi(\mathbf{z}^L|\mathbf{x}^L)\|p(\mathbf{z}^L)) + \mathbb{E}_{q_\phi(\mathbf{z}_\psi|\mathbf{x}^L)} \left[\|\mathbf{x}^H - D_\theta(\mathbf{z}^H)\|_2^2 \right], \end{aligned}$$

in which β is a hyperparameter adjusting the regularization KL term and also aligns with the β in Equation (3.8). Thus, the β in the decoder prior of Table 1 is analogous to the one in the BF-IB objective function in Equation (3.7), which also plays a similar role with β in β -VAE [42]. As we showed in Section 3.2, the value of β balances the tradeoff between the information compression and preservation from the perspective of IB and may be derived from prior knowledge or may be tuned using the validation error of the LF-VAE model.

As discussed in Section 3.1, the hyperparameter γ serves as the variance of the latent auto-regression. It indicates the degree of confidence in the accuracy of \mathbf{K}_ψ (defined in Equation (3.1)) when modeling the latent variables of the LF and HF models. A larger value of γ allows the auto-regression output to deviate further from \mathbf{K}_ψ , but also increases the variance of the ELBO gradients due to a more noisy reparameterized \mathbf{z}_ϵ^H as shown in Equation (3.6). In our numerical experiments, we observe that linear auto-regression in the latent space is capable of accurately capturing the relationship between the LF and HF latent representations, which means that we are able to choose γ to be small. Since a smaller γ ensures faster convergence when optimizing the HF-ELBO, we therefore choose $\gamma = 0$.

5. Empirical Results

In this section, we present empirical results obtained from the application of three PDE-based forward UQ problems. Specifically, the simulation of a composite beam is discussed in Section 5.1, followed by the examination of a thermally-driven cavity fluid flow with a high-dimensional uncertainty input in Section 5.2. Finally, a viscous Burgers’ equation is explored in Section 5.3. Regarding bi-fidelity modeling, the complexity of evaluating the LF models of these examples is assumed to be small compared to the HF models. We present the approximation behavior of our BF-VAE model, as well as the behavior of a HF-VAE model to provide a baseline for comparison. HF-VAE is a regular VAE as shown in Figure 2 that is trained solely with HF data and shares mirror priors and activation functions with BF-VAE. Our goal is to demonstrate the effectiveness of BF-VAE in utilizing LF information to synthesize HF QoI realizations in comparison to HF-VAEs. Our results demonstrate that BF-VAE provides a considerable advantage over HF-VAE when only a small number of HF samples can be afforded.¹

When evaluating a generative model, it is crucial to use an appropriate evaluation metric. While human evaluation may be adequate for determining the quality of outputs from models generating images and text, such an approach is not appropriate for evaluating the quality of PDE solutions. Therefore, we seek to identify a statistical distance that allows us to compare the difference between the true $p(\mathbf{x}^H)$ and the VAE surrogates $p_{\psi,\theta}(\mathbf{x}^H)$ without incurring excessive computational complexity. For deep generative models, there are two major evaluation options: Frechet inception distance (FID) [43] and kernel inception distance (KID) [44]. FID is most appropriate for evaluating image-based generative models using a pre-trained neural network, so in this study, we employ the KID, which stems from a

¹The code implementation is available at <https://github.com/CU-UQ/Bi-fidelity-VAE>.

statistical distance named maximum mean discrepancy (MMD) [45]. The KID values serve as an indicator of the deviation of the distribution of generated realizations from the distribution of true test data, which can be conveniently computed for high-dimensional samples. Given a non-negative and symmetric kernel function $k : \mathbb{R}^D \times \mathbb{R}^D \rightarrow \mathbb{R}$ and data $\{\mathbf{x}_i\}_{i=1}^T$ and $\{\mathbf{y}_i\}_{i=1}^T$, the KID is defined as

$$\begin{aligned} \text{KID}(\{\mathbf{x}_i\}_{i=1}^T, \{\mathbf{y}_j\}_{j=1}^T) &= \frac{1}{T(T-1)} \sum_{\substack{i,j=1 \\ i \neq j}}^T k(\mathbf{x}_i, \mathbf{x}_j) - \frac{2}{T^2} \sum_{i=1}^T \sum_{j=1}^T k(\mathbf{x}_i, \mathbf{y}_j) \\ &+ \frac{1}{T(T-1)} \sum_{\substack{i,j=1 \\ i \neq j}}^T k(\mathbf{y}_i, \mathbf{y}_j). \end{aligned} \tag{5.1}$$

Following [44], the kernel function we choose is the rational quadratic kernel

$$k_{\text{rq}}(\mathbf{x}_i, \mathbf{y}_j) := \sum_{\ell \in \mathcal{I}} \left(1 + \frac{\|\mathbf{x}_i - \mathbf{y}_j\|^2}{2\ell} \right)^{-\ell},$$

where $\mathcal{I} = \{0.2, 0.5, 1.0, 2.0, 5.0\}$ is a mixture of length scales to balance the bias effects from the different values. In order to evaluate the efficacy of the BF-VAE and HF-VAE models, we generated new realizations from the trained BF-VAE and HF-VAE models, denoted by $\{\mathbf{x}_i^{\text{BF}}\}_{i=1}^T, \{\mathbf{x}_j^{\text{HF}}\}_{j=1}^T$, respectively, where T is the test set size. The KIDs between the generated realizations and the true test data $\{\mathbf{x}_l^H\}_{l=1}^T$, which is not used for training, are computed as follows

$$\begin{aligned} \text{KID}^{\text{BF}} &:= \text{KID}(\{\mathbf{x}_l^H\}_{l=1}^T, \{\mathbf{x}_i^{\text{BF}}\}_{i=1}^T), \\ \text{KID}^{\text{HF}} &:= \text{KID}(\{\mathbf{x}_l^H\}_{l=1}^T, \{\mathbf{x}_j^{\text{HF}}\}_{j=1}^T). \end{aligned}$$

Further discussion and technical details regarding KID are presented in Appendix C. We also provide solution curves for 1,000 synthesized realizations generated by both the trained HF-VAE and BF-VAE models, along with their corresponding true HF QoI realizations for each numerical example. This additional result serves to further validate the KID outcomes. The hyperparameter β in Equation (3.8) is tuned to reduce the KID value of the LF-VAE and, as discussed in Section 4.2, γ in Equation (3.6) is assumed to be zero.

5.1. Composite Beam

Following [46, 47, 48, 49], we consider a plane-stress, cantilever beam with composite cross section and hollow web, as shown in Figure 5. The quantities of interest, in this case, are the displacements of the top cord at 128 equispaced points and represented as a vector with 128 entries. The uncertain inputs of the model are denoted as $\boldsymbol{\xi} = [\xi_1, \xi_2, \xi_3, \xi_4]$, where ξ_1, ξ_2 and ξ_3 are the Young's moduli of the three components of the cross section and ξ_4 is the intensity of the applied distributed force on the beam; see Figure 5. These are assumed to be statistically independent and uniformly distributed. The range of the input parameters, as well as the other deterministic parameters, are provided in Table 2.

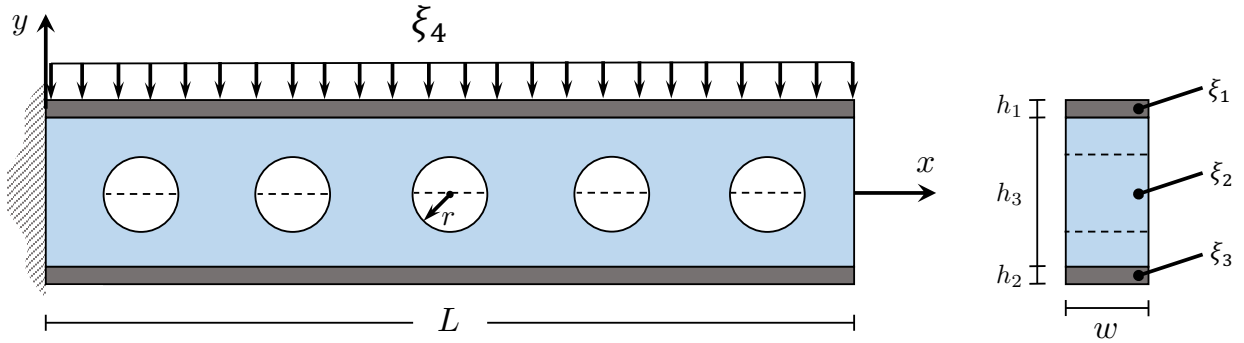


Figure 5: Cantilever beam (left) and the composite cross section (right) adapted from [46].

Table 2: The values of the parameters in the composite cantilever beam model. The centers of the holes are at $x = \{5, 15, 25, 35, 45\}$. The entries of ξ are drawn independently and uniformly at random from the specified intervals.

L	h_1	h_2	h_3	w	r	ξ_1	ξ_2	ξ_3	ξ_4
50	0.1	0.1	5	1	1.5	[0.9e6, 1.1e6]	[0.9e6, 1.1e6]	[0.9e4, 1.1e4]	[9, 11]

The HF QoI \mathbf{x}^H is based on a finite element discretization of the beam using a triangular mesh, as Figure 7 shows. The LF QoI \mathbf{x}^L is derived from the Euler–Bernoulli beam theory in which the vertical cross sections are assumed to remain planes throughout the deformation. The LF model ignores the shear deformation of the web and does not take the circular holes into account, which makes LF results smoother than HF results, as Figure 6 shows. Considering the Euler–Bernoulli theorem, the vertical displacement u is

$$EI_n \frac{d^4 u(x)}{dx^4} = -\xi_4, \quad (5.2)$$

where E and I_n are, respectively, the Young’s modulus and the moment of inertia of an equivalent cross section consisting of a single material. We let $E = \xi_3$, and the width of the top and bottom sections are $w_1 = (\xi_1/\xi_3)w$ and $w_2 = (\xi_2/\xi_3)w$, while all other dimensions are the same, as Figure 5 shows. The solution of (5.2) is

$$u(x) = -\frac{qL^4}{24EI_n} \left(\left(\frac{x}{L}\right)^4 - 4\left(\frac{x}{L}\right)^3 + 6\left(\frac{x}{L}\right)^2 \right).$$

The VAE models are implemented using fully-connected neural networks for both the encoder and decoder, each with two hidden layers and widths of 64 and 16 units, and ReLU activation functions. The latent space dimension is fixed at 4. The optimization of the VAE models is performed using the Adam optimizer with a learning rate of 1×10^{-3} and Adam-betas of 0.9 and 0.99. The batch size is set to 64, and the number of epochs for the initial

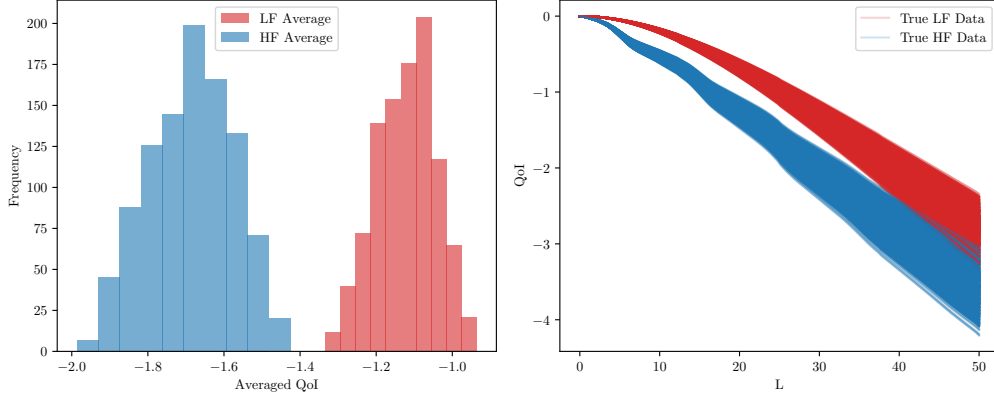


Figure 6: A histogram of the averaged QoI solutions along 128 spatial points from the LF and HF composite beam models is shown in the left figure, while 1,000 realizations of LF and HF QoIs are presented in the right figure.

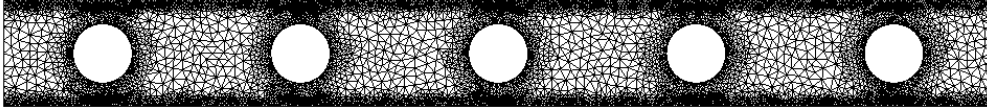


Figure 7: Finite element mesh used to generate HF solutions.

training of the LF-VAE (line 1 in Algorithm 1) is 2,000, followed by 1,000 for the BF-VAEs (line 4 in Algorithm 1). The hyperparameter β is 1.25.

An LF-VAE is first trained with $N = 4,000$ samples from $p(\mathbf{x}^L)$. A BF-VAE is built with parameters ϕ and θ initialized from the trained LF-VAE, as Algorithm 1 shows. We examine the performance of BF-VAE as a function of the number of HF data samples, with HF-VAE trained solely on the same HF samples as a baseline. The KID performance is evaluated using 1,000 test data and 1,000 samples from each of the trained VAEs across 10 trials, with the results averaged over the trials.

Figure 8 illustrates the KID performance of both the BF-VAE and HF-VAE, with the x-axis representing the number of HF data used for training and y-axis being KID values evaluated following Equation (5.1). The results show that KID^{BF} begins to converge with a small number of HF data, while KID^{HF} only starts to converge when the number of HF data exceeds 100. Given the practical limitations on the acquisition of HF data, the superiority of the BF-VAE model is thus evident. We also observe that when the size of HF data is large, e.g., more than 1,000, KID^{HF} surpasses KID^{BF} and achieves a better accuracy level. This is typical of multi-fidelity strategies and explanations are available in [47]. Figure 9 presents 1,000 realizations drawn from the trained HF-VAE and BF-VAE. We expect the displacement as a function of horizontal distance to be smooth and monotonic, but the HF-VAE samples fail to present these properties when $n < 1,000$ and thus, unphysical. It shows that BF-VAE is able to provide a reliable result with only a small amount of HF training

data, while HF-VAE requires more HF data to converge. Both figures demonstrate the effectiveness of the BF-VAE algorithm in utilizing the information from LF data to estimate the distribution of HF QoI.

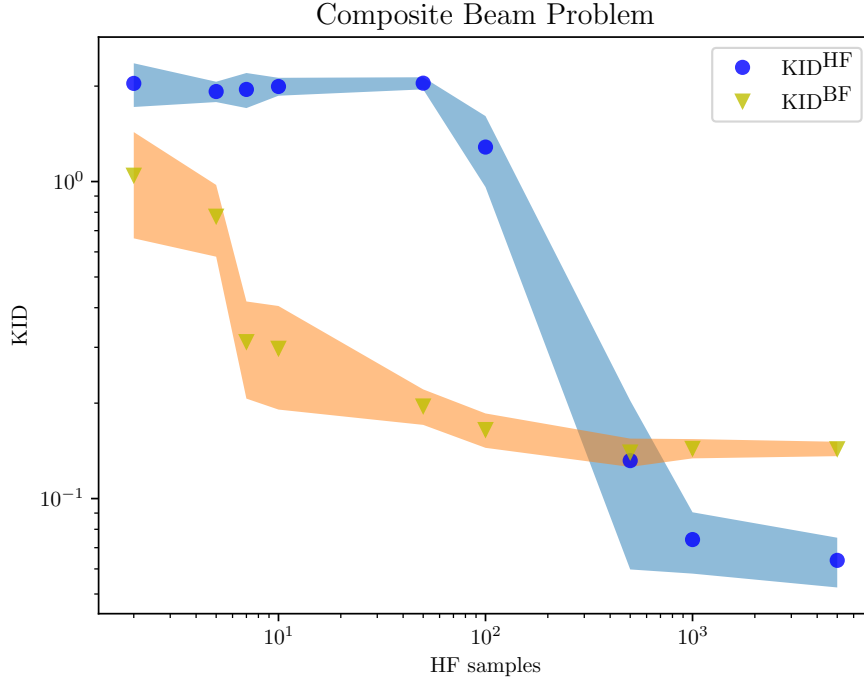


Figure 8: The KID results for the composite beam example given different sizes of HF data. Each circle represents the average KID between test data and the VAEs’ realizations over 10 separate trials. The shaded area is half the empirical standard deviation of these 10 trials.

5.2. Cavity Flow

Here we consider the case of temperature-driven fluid flow in a 2D cavity, with the quantity of interest being the heat flux along the hot wall as Figure 10 shows. The left-hand wall is considered the hot wall with a random temperature T_h , while the right-hand wall, referred to as the cold wall, has a smaller random temperature T_c with a constant mean of \bar{T}_c . The horizontal walls are treated as adiabatic. The reference temperature and the temperature difference are given by $T_{\text{ref}} = (T_h + \bar{T}_c)/2$ and $\Delta T_{\text{ref}} = T_h - \bar{T}_c$, respectively. The normalized governing equations are given by

$$\begin{aligned} \frac{\partial \mathbf{u}}{\partial t} + \mathbf{u} \cdot \nabla \mathbf{u} &= -\nabla p + \frac{\text{Pr}}{\sqrt{\text{Ra}}} \nabla^2 \mathbf{u} + \text{Pr} \Theta \mathbf{e}_y, \\ \nabla \cdot \mathbf{u} &= 0, \\ \frac{\partial \Theta}{\partial t} + \nabla \cdot (\mathbf{u} \Theta) &= \frac{1}{\sqrt{\text{Ra}}} \nabla^2 \Theta, \end{aligned}$$

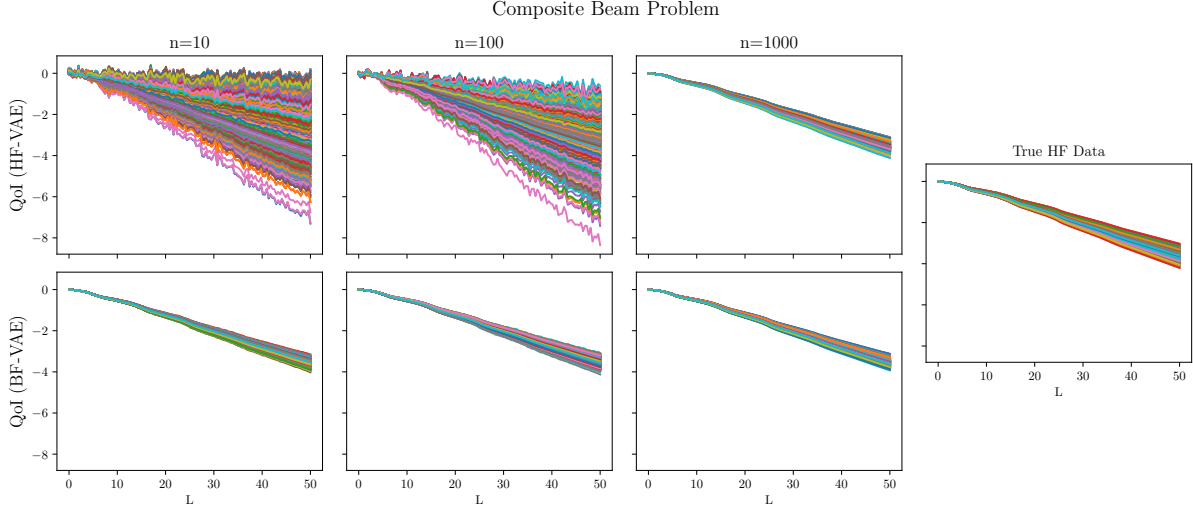


Figure 9: Comparison of 1,000 samples generated from the trained HF-VAE (top row), BF-VAE (bottom row) and the true HF model (right). A different number of HF data points are used in each of the first three columns: $n = 10$ (left column), $n = 100$ (middle left column), and $n = 1,000$ (middle right column).

where \mathbf{e}_y is the unit vector $(0, 1)$, $\mathbf{u} = (u, v)$ is the velocity vector field, $\Theta = (T - T_{\text{ref}})/\Delta T_{\text{ref}}$ is normalized temperature, p is pressure, and t is time. The walls are subject to no-slip boundary conditions. The dimensionless Prandtl and Rayleigh numbers are defined as $\text{Pr} = \nu_{\text{visc}}/\alpha$ and $\text{Ra} = g\tau\Delta T_{\text{ref}}W^3/(\nu_{\text{visc}}\alpha)$, respectively, where W is the width of the cavity, g is gravitational acceleration, ν_{visc} is kinematic viscosity, α is thermal diffusivity, and τ is the coefficient of thermal expansion. We set $g = 10$, $W = 1$, $\tau = 0.5$, $\Delta T_{\text{ref}} = 100$, $\text{Ra} = 10^6$, and $\text{Pr} = 0.71$. On the cold wall, we apply a temperature distribution with stochastic fluctuations as

$$T(x = 1, y) = \bar{T}_c + \sigma_T \sum_{i=1}^M \sqrt{\lambda_i} \varphi_i(y) \xi_i,$$

where $\bar{T}_c = 100$ is a constant, $\{\lambda_i\}_{i \in [M]}$ and $\{\varphi_i(y)\}_{i \in [M]}$ are the M largest eigenvalues and corresponding eigenfunctions of the kernel $k(y_1, y_2) = \exp(-|y_1 - y_2|/0.15)$, and each $\xi_i \stackrel{\text{i.i.d.}}{\sim} U[-1, 1]$. We let the input dimension M be 52 and $\sigma_T = 2$. The vector $\boldsymbol{\xi} = (\xi_1, \dots, \xi_{52})$ is the uncertain input of the model. These considerations align with previous works such as [50, 2, 51, 52, 53, 49].

Unlike the composite beam problem above, the fidelity levels of the cavity fluid flow problem are derived from the same PDE numerical solver but discretized on different grid resolutions. Specifically, we employ the finite volume method with a finer grid of size 256×256 to produce the HF QoI \mathbf{x}^H and a coarser grid of size 16×16 to produce the LF QoI \mathbf{x}^L . A comparison of LF and HF QoI are presented in Figure 11. Since the auto-encoder structure requires both LF and HF input data to have the same dimension, we interpolate the LF data

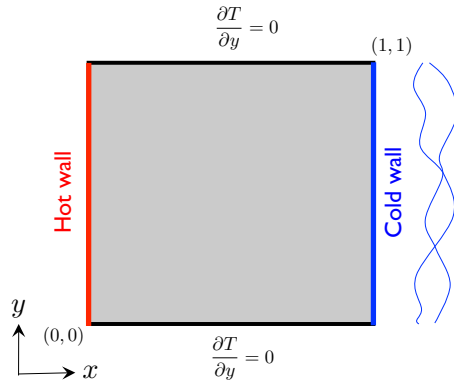


Figure 10: A figure of the temperature-driven cavity flow problem, reproduced from Figure 5 of [54].

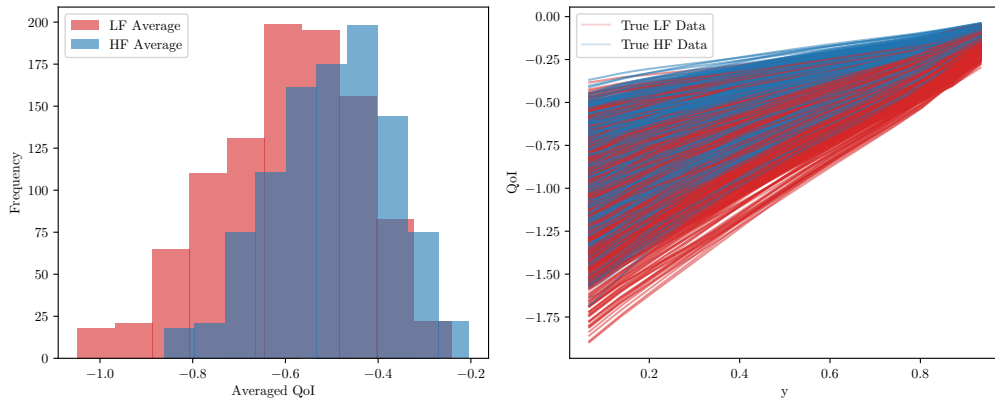


Figure 11: A histogram of the QoI solutions averaged on all spatial points from the LF and HF cavity flow models is shown in the left figure and 1,000 LF and HF QoIs are presented in the right figure.

linearly and let the QoI be the (interpolated) steady-state heat flux along the hot wall at 221 equispaced spots on $[0.067, 0.933]$, including the endpoints. For the VAE models, we use fully connected neural networks to model the encoder and decoder with ReLU activation functions, three hidden layers, and internal widths 221–128–64–16 determined by some preliminary tests. The dimension of the latent space is 4. The optimizer is Adam with a learning rate 1×10^{-3} and Adam-betas 0.9, 0.99. The batch size for the optimization is 64. The epoch number is 2,000 for the initial LF-VAE training (line 1 in Algorithm 1) followed by then 1,000 for BF-VAE training (line 4 in Algorithm 1). The number of LF data for training LF-VAE is $N = 4,000$. The value of the hyperparameter β is set to 4.5.

The average KID between real HF data and data generated by the HF-VAE and our BF-VAE, respectively, for different numbers of HF data points are shown in Figure 12. The averages are computed over 10 trials between 1,000 real data points and 1,000 VAE-simulated realizations. Newly generated realizations of HF-VAE and BF-VAE based on different HF training sample sizes are shown in Figure 13. The result of Figure 12 indicates that KID^{BF} is consistently lower than KID^{HF} but gets closer when more HF data is available. Figure 13 suggests that BF-VAE returns smoother and more reliable predictions compared to those of HF-VAEs, especially with limited HF training data, which means BF-VAE produces more realistic results. Both figures reveal that BF-VAE has better performance than HF-VAE when the two models are given the same amount of HF training data.

5.3. Burgers' Equation

The last example is a one-dimensional unsteady viscous Burgers' equation with uncertain initial condition and viscosity. The random velocity field $u(x, t, \boldsymbol{\xi})$ with parameters $\boldsymbol{\xi}$ is governed by

$$\begin{aligned} \frac{\partial u(x, t, \boldsymbol{\xi})}{\partial t} + u(x, t, \boldsymbol{\xi}) \frac{\partial u(x, t, \boldsymbol{\xi})}{\partial x} &= \frac{\partial}{\partial x} \left(\nu \frac{\partial u(x, t, \boldsymbol{\xi})}{\partial x} \right), \quad (x, t) \in [0, 1] \times [0, 2], \\ u(0, t, \boldsymbol{\xi}) &= u(1, t, \boldsymbol{\xi}) = 0, \\ u(x, 0, \boldsymbol{\xi}) &= g(x, \boldsymbol{\xi}), \quad x \in [0, 1], \end{aligned} \tag{5.3}$$

where the random viscosity ν is a shifted beta distribution $\text{Beta}(0.5, 5)$ in $[0.01, 0.05]$, and the initial condition $g(x, \boldsymbol{\xi})$ is

$$g(x, \boldsymbol{\xi}) = \sin(\pi x) + \sigma_g \sum_{k=2}^M \frac{1}{k} \sin(\pi k x) \xi_{k-1}. \tag{5.4}$$

The parameters in Equation (5.4) are $\sigma_g = 1.2840 \times 10^{-1}$ and $M = 6$. The random inputs $\xi_1, \xi_2, \dots, \xi_{M-1}$ are i.i.d. uniformly distributed between -1 and 1, resulting in a stochastic input vector $\boldsymbol{\xi} = [\xi_1, \xi_2, \dots, \xi_{M-1}, \nu]$. The QoIs are the values of $u(x, t = 2, \boldsymbol{\xi})$ at 254 equispaced x nodes between -1 and 1, excluding the boundary points. To generate bi-fidelity data, the discretization of the Equation (5.3) is carried out at two space/time grid sizes. The LF data is obtained using the semi-implicit, two-step Adam-Bashforth solver with a spatial

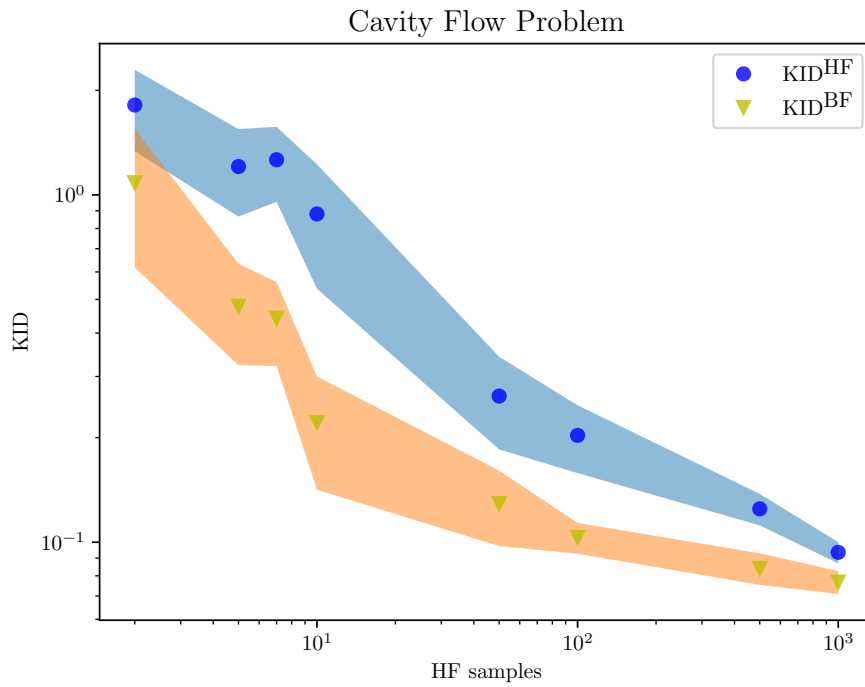


Figure 12: The KID result for the cavity flow problem given different sizes of HF data. Each point represents the average KID between test data and the VAEs' realizations over 10 separate trials. The shaded area corresponds to half the empirical standard deviation of these 10 trials.

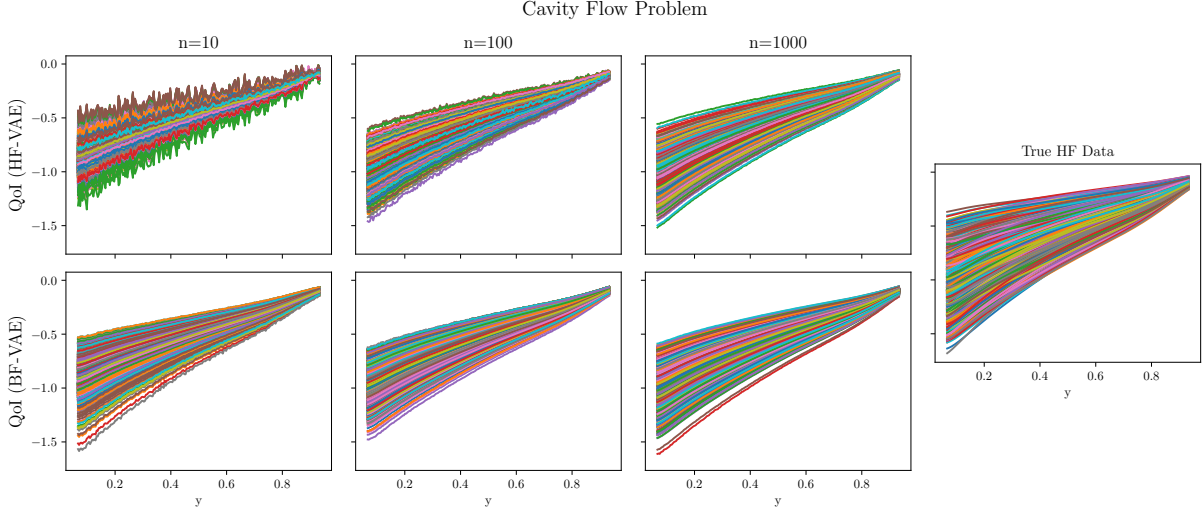


Figure 13: Comparison of 1,000 samples generated from the trained HF-VAE (top row), BF-VAE (bottom row) and the true HF model (right). A different number of HF data points are used in each of the first three columns: $n = 10$ (left column), $n = 100$ (middle left column), and $n = 1,000$ (middle right column).

grid of size $\Delta x = 1.176 \times 10^{-2}$ and time step size of $\Delta t = 2 \times 10^{-2}$. The same solver is applied for HF data, but with smaller space/time grid sizes, $\Delta x = 3.774 \times 10^{-3}$ and $\Delta t = 2 \times 10^{-4}$. The LF data is interpolated linearly on the finer grid so the dimensions of the LF and HF data are the same. A comparison between LF and HF data is presented in Figure 14.

For the VAE implementations, we use fully connected neural networks to model the encoder and decoder, with four hidden layers as 254–256–128–64–16. The dimension of the latent space is 16. As before, the Adam optimizer with a learning rate 1×10^{-3} and Adam-betas 0.9, 0.99 is applied. The batch size for the optimization is 64. The epoch number is 2,000 for the initial LF-VAE training (line 1 in Algorithm 1) with an additional 1,000 epochs for BF-VAE training (line 4 in Algorithm 1). We use $N = 4,000$ LF data points to train the LF-VAE. The value of hyperparameter β is set to 5×10^{-4} .

To validate the performance of the BF-VAE model, we compare its results with those of the HF-VAE model using KID. Compared with the previous two empirical examples, the LF and HF data of Burgers’ problem are more similar. For this reason, we investigate the experiment results of BF-VAE built on fewer HF data points in Figure 16. The KID results are computed as the average over ten trials consisting of 1,000 test data points and 1,000 VAE-generated data points, which are presented in Figure 15. Additionally, we demonstrate the validity of the BF-VAE model by generating realizations and comparing them with the HF-VAE counterparts, as shown in Figure 16. Based on our evaluation, we have observed that the BF-VAE model achieves a commendable level of accuracy in recovering the HF QoI compared with HF-VAE. Furthermore, it exhibits a more realistic pattern in accordance with physical rules, all while utilizing an impressively small set of HF data. Similarly to what we

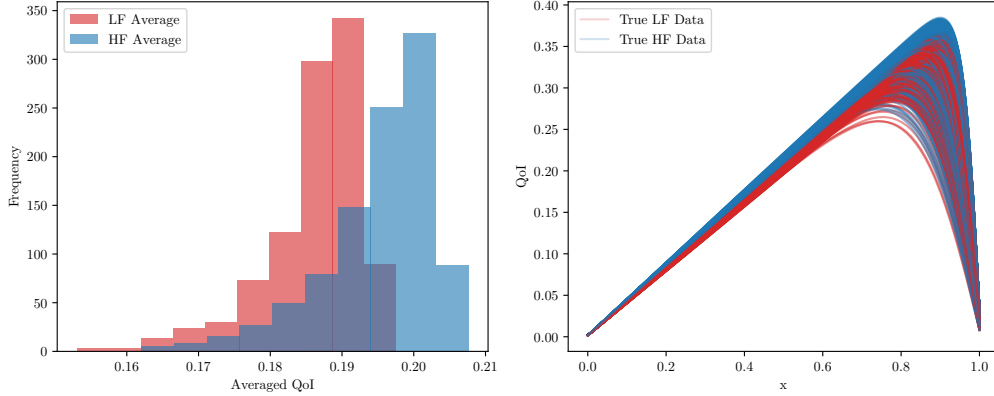


Figure 14: Histogram of the QoI values averaged on all spatial points from the LF and HF viscous Burgers’ models is shown in the left figure and 1,000 LF and HF QoIs are plotted in the right figure.

observed in Section 5.1, HF-VAE seems to outperform BF-VAE when a larger amount of HF data is available.

6. Conclusion

This paper presents a novel deep generative model, the bi-fidelity variational auto-encoder (BF-VAE), for estimating uncertainty through a bi-fidelity approach. The BF-VAE is independent of the dimension of the stochastic input and applicable to complex physical models. With an autoencoder architecture, BF-VAE exploits a low-dimensional latent space for the bi-fidelity auto-regression, which significantly reduces the number of high-fidelity (HF) samples required for training. Furthermore, a training criterion for BF-VAE is proposed and analyzed using information bottleneck theory [31]. The empirical experiments demonstrate the efficacy of the proposed algorithm in scenarios when the amount of HF data is limited.

VAE-based approaches, including those presented in this paper, typically impose a multivariate Gaussian distribution on the probabilistic encoder. As discussed in Section 3.3, this results in approximation errors. An interesting future research direction is to try using other deep generative models that do not suffer from this shortcoming in bi-fidelity UQ applications. Examples of promising models that have achieved state-of-the-art results in other domains include normalizing flows and diffusion models.

Acknowledgments

N. Cheng and A. Doostan were supported by the AFOSR awards FA9550-20-1-0138 and FA9550-20-1-0188 with Dr. Fariba Fahroo as the program manager. S. Becker was supported by DOE award DE-SC0023346. The views expressed in the article do not necessarily represent the views of the AFOSR or the U.S. Government.

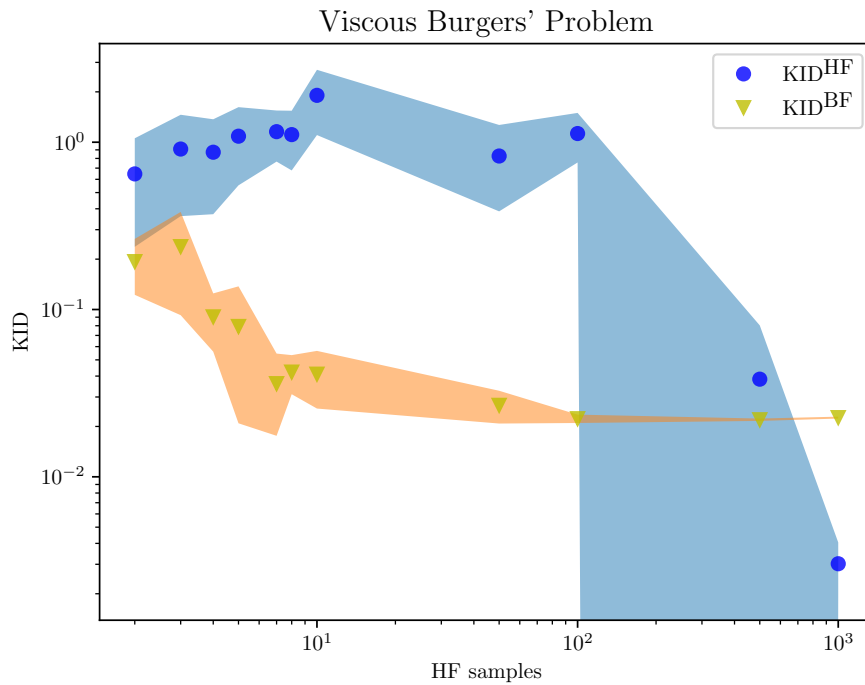


Figure 15: The KID result for the viscous Burgers' equation given different numbers of HF data points. Each point represents the average KID between the test data and the VAEs' realizations over 10 separate trials. The shaded area corresponds to half the empirical standard deviation of these 10 trials.

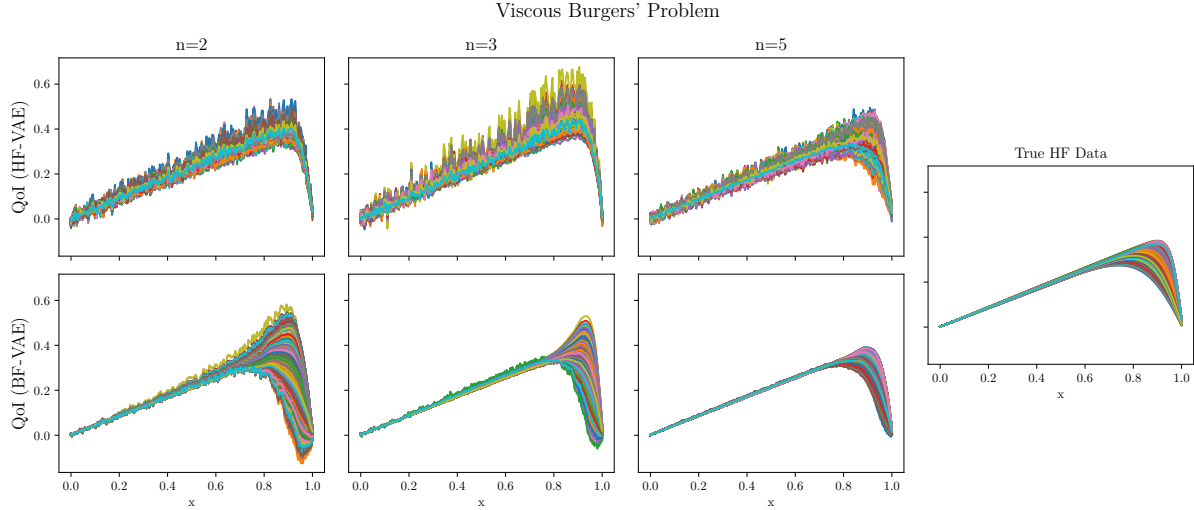


Figure 16: Comparison of 1,000 samples generated from the trained HF-VAE (top row), BF-VAE (bottom row) and the true HF model (right). A different number of HF data points are used in each of the first three columns: $n = 2$ (left column), $n = 3$ (middle left column), and $n = 5$ (middle right column).

References

- [1] R. G. Ghanem, P. D. Spanos, Stochastic finite elements: a spectral approach, Courier Corporation, 2003.
- [2] J. Peng, J. Hampton, A. Doostan, A weighted ℓ_1 -minimization approach for sparse polynomial chaos expansions, *Journal of Computational Physics* 267 (2014) 92–111.
- [3] J. Hampton, A. Doostan, Compressive sampling of polynomial chaos expansions: Convergence analysis and sampling strategies, *Journal of Computational Physics* 280 (2015) 363–386.
- [4] P. F. Shustin, S. Ubaru, V. Kalantzis, L. Horesh, H. Avron, PCENet: High dimensional surrogate modeling for learning uncertainty, arXiv preprint arXiv:2202.05063 (2022).
- [5] C. K. Williams, C. E. Rasmussen, Gaussian processes for machine learning, volume 2, MIT press Cambridge, MA, 2006.
- [6] I. Bilonis, N. Zabaras, Multi-output local gaussian process regression: Applications to uncertainty quantification, *Journal of Computational Physics* 231 (2012) 5718–5746.
- [7] R. K. Tripathy, I. Bilonis, Deep UQ: Learning deep neural network surrogate models for high dimensional uncertainty quantification, *Journal of Computational Physics* 375 (2018) 565–588.

- [8] Y. Zhu, N. Zabaras, P.-S. Koutsourelakis, P. Perdikaris, Physics-constrained deep learning for high-dimensional surrogate modeling and uncertainty quantification without labeled data, *Journal of Computational Physics* 394 (2019) 56–81.
- [9] G. A. Padmanabha, N. Zabaras, Solving inverse problems using conditional invertible neural networks, *Journal of Computational Physics* 433 (2021) 110194.
- [10] D. J. Lucia, P. S. Beran, W. A. Silva, Reduced-order modeling: New approaches for computational physics, *Progress in Aerospace Sciences* 40 (2004) 51–117.
- [11] A. Chatterjee, An introduction to the proper orthogonal decomposition, *Current Science* (2000) 808–817.
- [12] A. Pinkus, *N-widths in Approximation Theory*, volume 7, Springer Science & Business Media, 2012.
- [13] T. Zhou, Y. Peng, Kernel principal component analysis-based Gaussian process regression modelling for high-dimensional reliability analysis, *Computers & Structures* 241 (2020) 106358.
- [14] M. Razi, R. M. Kirby, A. Narayan, Kernel optimization for low-rank multifidelity algorithms, *International Journal for Uncertainty Quantification* 11 (2021).
- [15] Z. Zhang, H. Zha, Principal manifolds and nonlinear dimensionality reduction via tangent space alignment, *SIAM Journal on Scientific Computing* 26 (2004) 313–338.
- [16] K. Lee, K. T. Carlberg, Model reduction of dynamical systems on nonlinear manifolds using deep convolutional autoencoders, *Journal of Computational Physics* 404 (2020) 108973.
- [17] R. Maulik, B. Lusch, P. Balaprakash, Reduced-order modeling of advection-dominated systems with recurrent neural networks and convolutional autoencoders, *Physics of Fluids* 33 (2021) 037106.
- [18] S. Nikolopoulos, I. Kalogeris, V. Papadopoulos, Non-intrusive surrogate modeling for parametrized time-dependent partial differential equations using convolutional autoencoders, *Engineering Applications of Artificial Intelligence* 109 (2022) 104652.
- [19] H. Steck, Autoencoders that don’t overfit towards the identity, *Advances in Neural Information Processing Systems* 33 (2020) 19598–19608.
- [20] Y. Zhu, N. Zabaras, Bayesian deep convolutional encoder–decoder networks for surrogate modeling and uncertainty quantification, *Journal of Computational Physics* 366 (2018) 415–447.
- [21] N. Geneva, N. Zabaras, Modeling the dynamics of PDE systems with physics-constrained deep auto-regressive networks, *Journal of Computational Physics* 403 (2020) 109056.

- [22] D. P. Kingma, M. Welling, Auto-encoding variational bayes, arXiv preprint arXiv:1312.6114 (2013).
- [23] D. J. Rezende, S. Mohamed, D. Wierstra, Stochastic backpropagation and approximate inference in deep generative models, in: International Conference on Machine Learning, PMLR, 2014, pp. 1278–1286.
- [24] I. Goodfellow, J. Pouget-Abadie, M. Mirza, B. Xu, D. Warde-Farley, S. Ozair, A. Courville, Y. Bengio, Generative adversarial networks, Communications of the ACM 63 (2020) 139–144.
- [25] D. Rezende, S. Mohamed, Variational inference with normalizing flows, in: International Conference on Machine Learning, PMLR, 2015, pp. 1530–1538.
- [26] J. Ho, A. Jain, P. Abbeel, Denoising diffusion probabilistic models, Advances in Neural Information Processing Systems 33 (2020) 6840–6851.
- [27] Y. Song, J. Sohl-Dickstein, D. P. Kingma, A. Kumar, S. Ermon, B. Poole, Score-based generative modeling through stochastic differential equations, arXiv preprint arXiv:2011.13456 (2020).
- [28] Z. Wang, Q. She, T. E. Ward, Generative adversarial networks in computer vision: A survey and taxonomy, ACM Computing Surveys (CSUR) 54 (2021) 1–38.
- [29] M. Petrovich, M. J. Black, G. Varol, Action-conditioned 3D human motion synthesis with transformer VAE, in: Proceedings of the IEEE/CVF International Conference on Computer Vision, 2021, pp. 10985–10995.
- [30] S. Rajeswar, S. Subramanian, F. Dutil, C. Pal, A. Courville, Adversarial generation of natural language, arXiv preprint arXiv:1705.10929 (2017).
- [31] N. Tishby, F. C. Pereira, W. Bialek, The information bottleneck method, arXiv preprint physics/0004057 (2000).
- [32] J. Nitzler, J. Biehler, N. Fehn, P.-S. Koutsourelakis, W. A. Wall, A generalized probabilistic learning approach for multi-fidelity uncertainty quantification in complex physical simulations, Computer Methods in Applied Mechanics and Engineering 400 (2022) 115600.
- [33] D. M. Blei, A. Kucukelbir, J. D. McAuliffe, Variational inference: A review for statisticians, Journal of the American statistical Association 112 (2017) 859–877.
- [34] W. Chen, P. Stinis, Feature-adjacent multi-fidelity physics-informed machine learning for partial differential equations, arXiv preprint arXiv:2303.11577 (2023).
- [35] M. C. Kennedy, A. O’Hagan, Predicting the output from a complex computer code when fast approximations are available, Biometrika 87 (2000) 1–13.

- [36] M. C. Kennedy, A. O’Hagan, Bayesian calibration of computer models, *Journal of the Royal Statistical Society: Series B (Statistical Methodology)* 63 (2001) 425–464.
- [37] L. Le Gratiet, Multi-fidelity Gaussian process regression for computer experiments, Ph.D. thesis, Université Paris-Diderot-Paris VII, 2013.
- [38] R. Shwartz-Ziv, N. Tishby, Opening the black box of deep neural networks via information, arXiv preprint arXiv:1703.00810 (2017).
- [39] T. M. Cover, *Elements of information theory*, John Wiley & Sons, 1999.
- [40] K. P. Murphy, *Probabilistic Machine Learning: Advanced Topics*, MIT Press, 2023.
- [41] A. Shekhovtsov, D. Schlesinger, B. Flach, VAE approximation error: ELBO and exponential families, arXiv preprint arXiv:2102.09310 (2021).
- [42] I. Higgins, L. Matthey, A. Pal, C. Burgess, X. Glorot, M. Botvinick, S. Mohamed, A. Lerchner, beta-VAE: Learning basic visual concepts with a constrained variational framework, *International Conference on Learning Representations* (2017).
- [43] M. Heusel, H. Ramsauer, T. Unterthiner, B. Nessler, S. Hochreiter, GANs trained by a two time-scale update rule converge to a local nash equilibrium, *Advances in Neural Information Processing Systems* 30 (2017).
- [44] M. Bińkowski, D. J. Sutherland, M. Arbel, A. Gretton, Demystifying MMD GANs, arXiv preprint arXiv:1801.01401 (2018).
- [45] A. Gretton, K. M. Borgwardt, M. J. Rasch, B. Schölkopf, A. Smola, A kernel two-sample test, *Journal of Machine Learning Research* 13 (2012) 723–773.
- [46] J. Hampton, H. R. Fairbanks, A. Narayan, A. Doostan, Practical error bounds for a non-intrusive bi-fidelity approach to parametric/stochastic model reduction, *Journal of Computational Physics* 368 (2018) 315–332.
- [47] S. De, J. Britton, M. Reynolds, R. Skinner, K. Jansen, A. Doostan, On transfer learning of neural networks using bi-fidelity data for uncertainty propagation, *International Journal for Uncertainty Quantification* 10 (2020).
- [48] S. De, A. Doostan, Neural network training using ℓ_1 -regularization and bi-fidelity data, *Journal of Computational Physics* 458 (2022) 111010.
- [49] N. Cheng, O. A. Malik, Y. Xu, S. Becker, A. Doostan, A. Narayan, Quadrature sampling of parametric models with bi-fidelity boosting, arXiv preprint arXiv:2209.05705 (2022).
- [50] M. Bachmayr, A. Cohen, Kolmogorov widths and low-rank approximations of parametric elliptic PDEs, *Mathematics of Computation* 86 (2017) 701–724.

- [51] J. Hampton, A. Doostan, Compressive sampling of polynomial chaos expansions: Convergence analysis and sampling strategies, *Journal of Computational Physics* 280 (2015) 363–386.
- [52] J. Hampton, A. Doostan, Coherence motivated sampling and convergence analysis of least squares polynomial chaos regression, *Computer Methods in Applied Mechanics and Engineering* 290 (2015) 73–97.
- [53] J. Hampton, A. Doostan, Basis adaptive sample efficient polynomial chaos (BASE-PC), *Journal of Computational Physics* 371 (2018) 20–49.
- [54] H. R. Fairbanks, A. Doostan, C. Ketelsen, G. Iaccarino, A low-rank control variate for multilevel Monte Carlo simulation of high-dimensional uncertain systems, *Journal of Computational Physics* 341 (2017) 121–139.
- [55] C. Villani, *Topics in optimal transportation*, volume 58, American Mathematical Soc., 2021.

Appendix A. Proof of Bi-fidelity ELBO

In this section, we present the detailed proof of Equation (3.2). We assume the Markov property for the BF-VAE so that $p(\mathbf{x}^H | \mathbf{z}^L, \mathbf{z}^H) = p(\mathbf{x}^H | \mathbf{z}^H)$ and $p(\mathbf{z}^H | \mathbf{z}^L, \mathbf{x}^L) = p(\mathbf{z}^H | \mathbf{z}^L)$.

Proof. HF log-likelihood $\log p_{\theta, \psi}(\mathbf{x}^H)$ can be decomposed and lower bounded as follows

$$\begin{aligned}
\log p_{\theta, \psi}(\mathbf{x}^H) &= \mathbb{E}_{q_{\phi}(\mathbf{z}_{\psi} | \mathbf{x}^L)} [\log p_{\theta, \psi}(\mathbf{x}^H)] \\
&= \mathbb{E}_{q_{\phi}(\mathbf{z}_{\psi} | \mathbf{x}^L)} \left[\log \left(\frac{p_{\theta}(\mathbf{x}^H, \mathbf{z}_{\psi})}{p_{\theta}(\mathbf{z}_{\psi} | \mathbf{x}^H)} \right) \right] \\
&= \mathbb{E}_{q_{\phi}(\mathbf{z}_{\psi} | \mathbf{x}^L)} \left[\log \left(\frac{p_{\theta}(\mathbf{x}^H, \mathbf{z}_{\psi}) q_{\phi}(\mathbf{z}_{\psi} | \mathbf{x}^L)}{p_{\theta}(\mathbf{z}_{\psi} | \mathbf{x}^H) q_{\phi}(\mathbf{z}_{\psi} | \mathbf{x}^L)} \right) \right] \\
&= \text{KL}(q_{\phi}(\mathbf{z}_{\psi} | \mathbf{x}^L) \| p_{\theta}(\mathbf{z}_{\psi} | \mathbf{x}^H)) + \mathbb{E}_{q_{\phi}(\mathbf{z}_{\psi} | \mathbf{x}^L)} \left[\log \left(\frac{p_{\theta}(\mathbf{x}^H, \mathbf{z}_{\psi})}{q_{\phi}(\mathbf{z}_{\psi} | \mathbf{x}^L)} \right) \right] \\
&\geq \mathbb{E}_{q_{\phi}(\mathbf{z}_{\psi} | \mathbf{x}^L)} \left[\log \left(\frac{p_{\theta}(\mathbf{x}^H, \mathbf{z}_{\psi})}{q_{\phi}(\mathbf{z}_{\psi} | \mathbf{x}^L)} \right) \right] \\
&= \mathbb{E}_{q_{\phi}(\mathbf{z}_{\psi} | \mathbf{x}^L)} \left[\log \left(\frac{p_{\theta}(\mathbf{x}^H | \mathbf{z}_{\psi}) p_{\psi}(\mathbf{z}^H | \mathbf{z}^L) p(\mathbf{z}^L)}{p_{\psi}(\mathbf{z}^H | \mathbf{z}^L) q_{\phi}(\mathbf{z}^L | \mathbf{x}^L)} \right) \right] \\
&= \mathbb{E}_{q_{\phi}(\mathbf{z}_{\psi} | \mathbf{x}^L)} \left[\log \left(\frac{p(\mathbf{z}^L)}{q_{\phi}(\mathbf{z}^L | \mathbf{x}^L)} \right) + \log(p_{\theta}(\mathbf{x}^H | \mathbf{z}_{\psi})) \right] \\
&= -\text{KL}(q_{\phi}(\mathbf{z}^L | \mathbf{x}^L) \| p(\mathbf{z}^L)) + \mathbb{E}_{q_{\phi}(\mathbf{z}_{\psi} | \mathbf{x}^L)} [\log(p_{\theta}(\mathbf{x}^H | \mathbf{z}_{\psi}))] \\
&= \text{ELBO}^{\text{BF}}(\phi, \psi, \theta).
\end{aligned}$$

The only inequality above follows from the non-negativity of KL divergence. The above derivation shows that the HF log-likelihood can be lower bounded by the proposed BF-ELBO in Equation (3.3), where the tightness of the bound is controlled by the approximation error mentioned in Section 3.3 as $\text{KL}(q_{\phi}(\mathbf{z}_{\psi} | \mathbf{x}^L) \| p_{\theta}(\mathbf{z}_{\psi} | \mathbf{x}^H))$. \square

Appendix B. Proof of Bi-fidelity Information Bottleneck

In this section, we prove that optimizing $\text{ELBO}^{\text{BF}}(\phi, \psi, \theta)$ in Equation (3.3) is equivalent with optimizing BF-IB objective function $\text{IB}_{\beta}^{\text{BF}}$ in Equation (3.7) with $\beta = 1$. With the BF-IB graphical model $\mathbf{z}_{\psi} \leftarrow \mathbf{x}^L \leftrightarrow \mathbf{x}^H$ assumed (similar with IB in [40]), we have $q_{\phi}(\mathbf{z}_{\psi} | \mathbf{x}^L) = q_{\phi}(\mathbf{z}_{\psi} | \mathbf{x}^L, \mathbf{x}^H)$.

Proof.

$$\begin{aligned}
& \text{IB}^{\text{BF}}(\phi, \psi, \theta) \\
&= -\mathbb{I}(\mathbf{x}^L, \mathbf{z}_\psi) + \mathbb{I}(\mathbf{z}_\psi, \mathbf{x}^H) \\
&= -\mathbb{E}_{p(\mathbf{x}^L, \mathbf{z}_\psi)} \left[\log \frac{q_\phi(\mathbf{z}_\psi, \mathbf{x}^L)}{p(\mathbf{z}_\psi)p(\mathbf{x}^L)} \right] + \mathbb{E}_{p(\mathbf{x}^H, \mathbf{z}_\psi)} \left[\log \frac{p_\theta(\mathbf{x}^H, \mathbf{z}_\psi)}{p(\mathbf{x}^H)p(\mathbf{z}_\psi)} \right] \\
&= -\mathbb{E}_{p_\phi(\mathbf{x}^L, \mathbf{z}_\psi)} \left[\log \frac{q_\phi(\mathbf{z}_\psi | \mathbf{x}^L)}{p_\psi(\mathbf{z}_\psi)} \right] + \mathbb{E}_{p(\mathbf{x}^H, \mathbf{z}_\psi)} [\log p_\theta(\mathbf{x}^H | \mathbf{z}_\psi)] + \mathbb{H}[\mathbf{x}^H] \\
&= -\mathbb{E}_{p(\mathbf{x}^L, \mathbf{z}^H, \mathbf{z}^L)} \left[\log \frac{q_\phi(\mathbf{z}^L | \mathbf{x}^L)p_\psi(\mathbf{z}^H | \mathbf{z}^L)}{p(\mathbf{z}^L)p_\psi(\mathbf{z}^H | \mathbf{z}^L)} \right] + \mathbb{E}_{p(\mathbf{x}^H, \mathbf{z}^H, \mathbf{z}^L)} [\log p_\theta(\mathbf{x}^H | \mathbf{z}^H)] + \mathbb{H}[\mathbf{x}^H] \\
&= -\mathbb{E}_{p(\mathbf{x}^L)} \left[\text{KL}(q_\phi(\mathbf{z}^L | \mathbf{x}^L) || p(\mathbf{z}^L)) \right] + \mathbb{E}_{p(\mathbf{x}^H, \mathbf{z}^H, \mathbf{z}^L)} \left[\log p_\theta(\mathbf{x}^H | \mathbf{z}^H) \right] + \mathbb{H}[\mathbf{x}^H] \\
&= -\mathbb{E}_{p(\mathbf{x}^L)} \left[\text{KL}(q_\phi(\mathbf{z}^L | \mathbf{x}^L) || p(\mathbf{z}^L)) \right] + \int p(\mathbf{x}^H, \mathbf{z}^H, \mathbf{z}^L) \left[\log p_\theta(\mathbf{x}^H | \mathbf{z}^H) \right] d\mathbf{z}^L d\mathbf{z}^H d\mathbf{x}^H + \mathbb{H}[\mathbf{x}^H] \\
&= -\mathbb{E}_{p(\mathbf{x}^L)} \left[\text{KL}(q_\phi(\mathbf{z}^L | \mathbf{x}^L) || p(\mathbf{z}^L)) \right] \\
&\quad + \int q_\phi(\mathbf{z}^L, \mathbf{z}^H | \mathbf{x}^L, \mathbf{x}^H) p(\mathbf{x}^H, \mathbf{x}^L) \left[\log p_\theta(\mathbf{x}^H | \mathbf{z}^H) \right] d\mathbf{z}^H d\mathbf{x}^H d\mathbf{x}^L d\mathbf{z}^L + \mathbb{H}[\mathbf{x}^H] \\
&= -\mathbb{E}_{p(\mathbf{x}^L)} \left[\text{KL}(q_\phi(\mathbf{z}^L | \mathbf{x}^L) || p(\mathbf{z}^L)) \right] \\
&\quad + \int q_\phi(\mathbf{z}^L | \mathbf{x}^L) p(\mathbf{x}^H, \mathbf{x}^L) p_\psi(\mathbf{z}^H | \mathbf{z}^L) \left[\log p_\theta(\mathbf{x}^H | \mathbf{z}^H) \right] d\mathbf{z}^H d\mathbf{x}^H d\mathbf{x}^L d\mathbf{z}^L + \mathbb{H}[\mathbf{x}^H] \\
&= -\mathbb{E}_{p(\mathbf{x}^L)} \left[\text{KL}(q_\phi(\mathbf{z}^L | \mathbf{x}^L) || p(\mathbf{z}^L)) \right] + \mathbb{E}_{p(\mathbf{x}^L, \mathbf{x}^H)} \mathbb{E}_{q_\phi(\mathbf{z}^L | \mathbf{x}^L)} \left[\mathbb{E}_{p_\psi(\mathbf{z}^H | \mathbf{z}^L)} [\log p_\theta(\mathbf{x}^H | \mathbf{z}^H)] \right] + \mathbb{H}[\mathbf{x}^H] \\
&= \mathbb{E}_{p(\mathbf{x}^L, \mathbf{x}^H)} [\text{ELBO}^{\text{BF}}(\phi, \psi, \theta)] + \text{constant},
\end{aligned}$$

where $\mathbb{H}[\cdot]$ is the differential entropy of the input random vector. Since $p(\mathbf{x}^H)$ is fixed, its entropy is a constant. \square

Appendix C. A Brief Introduction to KID

In this section, we briefly introduce the kernel inception score (KID). KID is a commonly-used metric for evaluating the performance of generative models [44], which stems from maximum mean discrepancy (MMD). MMD is a type of statistical distance that falls under the umbrella of the integral probability metric (IPM). Given two probability distributions $p(\mathbf{x})$ and $q(\mathbf{x})$, the IPM is defined as

$$\text{IPM}_{\mathcal{F}}(p, q) := \sup_{f \in \mathcal{F}} \mathbb{E}_p[f(\mathbf{x})] - \mathbb{E}_q[f(\mathbf{x})],$$

where the function class \mathcal{F} controls the value range of the IPM and \mathbb{E}_p is the expectation with respect to the density $p(\mathbf{x})$. Larger \mathcal{F} brings higher accuracy to the IPM value but also increases the computing complexity. By Kantorovich-Rubinstein duality theorem [55],

the Wasserstein-1 distance is a type of IPM with \mathcal{F} being all Lipschitz continuous functions having Lipschitz constant bounded by 1. However, estimating the Wasserstein distance accurately in many dimensions is difficult. MMD assigns \mathcal{F} to be all functions in a reproducing kernel Hilbert space (RKHS) \mathcal{H} with norm bounded by 1, where \mathcal{H} is generated from a given kernel function $k : \mathbb{R}^D \times \mathbb{R}^D \rightarrow \mathbb{R}$. The motivation for using RKHS is for its computational convenience, as the following propositions show.

Proposition Appendix C.1. *MMD can be expressed in the following alternative form.*

$$\begin{aligned} \text{MMD}(p, q) &:= \sup_{\|f\|_{\mathcal{H}}=1} \mathbb{E}_p[f(\mathbf{x})] - \mathbb{E}_q[f(\mathbf{x})] \\ &= \|\mathcal{G}_{\mathcal{H}}(p) - \mathcal{G}_{\mathcal{H}}(q)\|_{\mathcal{H}}, \end{aligned}$$

where $\mathcal{G}_{\mathcal{H}}$ is a Bochner integral defined as $\mathcal{G}_{\mathcal{H}}(p) := \int_{\mathbb{R}^D} k(\mathbf{x}, \cdot) p(\mathbf{x}) d\mathbf{x}$.

The proof of Proposition Appendix C.1 is available from the Lemma 4 in [45]. Suppose we have samples $\{\mathbf{x}_i\}_{i=1}^m \sim p(\mathbf{x})$ and $\{\tilde{\mathbf{x}}_i\}_{i=1}^n \sim q(\mathbf{x})$, an unbiased estimator of MMD^2 , named KID, is as follow by Proposition Appendix C.1.

$$\begin{aligned} \text{KID}(\{\mathbf{x}_i\}_{i=1}^m, \{\tilde{\mathbf{x}}_i\}_{i=1}^n) & \tag{C.1} \\ &= \frac{1}{m(m-1)} \sum_{\substack{i,j=1 \\ i \neq j}}^m k(\mathbf{x}_i, \mathbf{x}_j) - \frac{2}{mn} \sum_{i=1}^m \sum_{j=1}^n k(\mathbf{x}_i, \tilde{\mathbf{x}}_j) + \frac{1}{n(n-1)} \sum_{\substack{i,j=1 \\ i \neq j}}^n k(\tilde{\mathbf{x}}_i, \tilde{\mathbf{x}}_j). \end{aligned}$$

Equation (C.1) discloses the connection between KID and MMD. In Section 5, we use KID to present the distributional similarity between two given samples.

The authors of [44] have shown that a rational quadratic kernel with a mixture of length scales is a superior candidate for MMD, due to its low rate of tail decay. The rational quadratic kernel has the form

$$k_{\text{rq}}(\mathbf{x}_i, \mathbf{y}_j) := \sum_{\ell \in \mathcal{I}} \left(1 + \frac{\|\mathbf{x}_i - \mathbf{y}_j\|^2}{2\ell} \right)^{-\ell},$$

where $\mathcal{I} = [0.2, 0.5, 1.0, 2.0, 5.0]$ is a mixture of different length scales.

The following results, which appear as Theorem 10 and Corollary 16 in [45], show the consistency of KID.

Proposition Appendix C.2. *Assuming both input sample sets have the same size m , and that the kernel function satisfies $0 \leq k(\mathbf{x}, \mathbf{y}) \leq K$, KID in Equation (C.1) satisfies*

$$\begin{aligned} \mathbb{P}[|\text{KID} - \text{MMD}^2| > \epsilon] &\leq 2 \exp\left(-\frac{\epsilon^2 m}{16K^2}\right), \\ m^{1/2}(\text{KID} - \text{MMD}^2) &\xrightarrow{d} \mathcal{N}(0, \sigma_u^2), \end{aligned}$$

where σ_u^2 is a value independent of m and D .

It should be noted that the asymptotic mean square error of KID is $m^{-1}\sigma_u^2$, which is independent of dimension D . It is the key reason why we choose KID over other statistical distances to test our models, considering the problems in this work have large D ($D \geq 100$).